Computational Condensed Matter 44 (2025) e01083

Contents lists available at ScienceDirect

Computational Condensed Matter

journal homepage: www.elsevier.com/locate/cocom

Enhanced thermoelectric performance of double perovskites Ba_2NbBiS_6 and Ba_2TaSbS_6 via carrier engineering and chemical potential tuning

T. Ghellab [a,b], H. Baaziz [a,b,*], Z. Charifi [a,b]

[a] Department of Physics, Faculty of Science, University of M'sila, 28000, M'sila, Algeria
[b] Laboratory of Physics and Chemistry of Materials, University of M'sila, Algeria

ARTICLE INFO

Keywords:
Double perovskites
Thermoelectric properties
Figure of merit (ZT)
Elastic properties
Carrier concentration tuning
High-temperature applications
Ba_2NbBiS_6
Ba_2TaSbS_6

ABSTRACT

The elastic and thermoelectric properties of Ba_2NbBiS_6 and Ba_2TaSbS_6 were investigated to assess their mechanical stability and thermoelectric efficiency. Elastic property calculations confirmed that both compounds satisfy the mechanical stability criteria. Ba_2TaSbS_6 exhibits a higher bulk modulus (127.34 GPa), shear modulus (54.92 GPa), and Young's modulus (139.83 GPa), indicating superior stiffness and hardness, while Ba_2NbBiS_6, with a lower bulk modulus (112.51 GPa) and shear modulus (48.76 GPa), demonstrates greater ductility, making it more adaptable for flexible applications.

Thermoelectric transport properties were analyzed as functions of temperature, carrier concentration, and chemical potential. At 900 K, Ba_2NbBiS_6 exhibited an initial ZT of 0.6090 at a carrier concentration of $n_0 = -3.2920 \times 10^{19}$ cm^{-3} and chemical potential $\mu_0 = 0.5411$ Ryd, while Ba_2TaSbS_6 had a ZT of 0.4968 at $n_0 = 0.9666 \times 10^{19}$ cm^{-3} and $\mu_0 = 0.62138$ Ryd. An increase in ZT was observed with temperature, attributed to enhanced charge carrier mobility and reduced lattice thermal conductivity. A systematic optimization of carrier concentration through controlled doping led to significant enhancements in ZT, reaching 0.9209 for Ba_2NbBiS_6 at $n = -23.6592 \times 10^{21}$ cm^{-3} and $\mu = \mu_0 + 0.1782$ Ryd, and 0.8646 for Ba_2TaSbS_6 at $n = -1.6144 \times 10^{21}$ cm^{-3} with $\mu = \mu_0 + 0.1073$ Ryd, representing increases of 51.2 % and 74.1 %, respectively. These findings highlight the potential of Ba_2NbBiS_6 and Ba_2TaSbS_6 for high-temperature thermoelectric applications, where a balance between mechanical stability and energy efficiency is crucial. Ba_2TaSbS_6 stands out as a mechanically robust material suitable for high-strength applications, while Ba_2NbBiS_6, with its enhanced ductility, is promising for flexible thermoelectric devices. Future studies should explore doping strategies and nanostructuring techniques to further enhance their thermoelectric properties for practical energy conversion applications.

1. Introduction

Perovskite-based materials, particularly double perovskites, have emerged as a highly versatile class of compounds due to their diverse structural, electronic, and functional properties. These materials are widely explored for applications in optoelectronics, photovoltaics, and thermoelectrics [1,2]. Among them, chalcogenide-based double perovskites have gained significant attention owing to their enhanced stability, strong spin-orbit coupling, and tunable bandgap properties, which are critical for high-performance semiconductor and thermoelectric applications [3,4]. The ability to tailor these materials through chemical substitution and structural modifications has opened new avenues for optimizing their electronic and transport properties, making them promising candidates for next-generation technologies [5,6].

Double perovskites, with the general formula $A_2BB'X_6$ (where A is an alkaline-earth or rare-earth metal, B and B′ are transition metals or main-group elements, and X is a chalcogen or halogen), exhibit unique structural characteristics that distinguish them from conventional perovskites. The ordered arrangement of B and B′ cations within the octahedral framework introduces strong electronic correlations, spin-orbit coupling effects, and tailored bandgap engineering, making them ideal for optoelectronic and thermoelectric applications [7,8]. Furthermore, the flexibility in cation selection allows for fine-tuning of physical properties such as charge transport, phonon dynamics, and mechanical stability, which are essential for energy harvesting and storage technologies [9,10].

Recent studies have identified Ba_2NbBiS_6 and Ba_2TaSbS_6 as promising semiconducting chalcogenide-based double perovskites. First-

* Corresponding author. Department of Physics, Faculty of Science, University of M'sila, 28000, M'sila, Algeria.
E-mail addresses: baaziz_hakim@yahoo.fr, hakim.baaziz@univ-msila.dz (H. Baaziz).

https://doi.org/10.1016/j.cocom.2025.e01083
Received 23 April 2025; Received in revised form 17 June 2025; Accepted 19 June 2025
Available online 19 June 2025

principles density functional theory (DFT) calculations reveal indirect bandgaps of 1.680 eV and 1.529 eV, respectively, suggesting their potential for applications in photodetectors, light-emitting devices, and power electronics [11]. These materials also exhibit strong absorption in the ultraviolet (UV) spectral range, as evidenced by their optical properties, including dielectric function, reflectivity, refractive index, and absorption spectrum. Additionally, structural stability and compressibility studies indicate that Ba_2TaSbS_6 demonstrates higher resistance to compression compared to Ba_2NbBiS_6, further highlighting its potential for robust device integration [11].

Despite significant progress in understanding the structural, electronic, and optical properties of these materials, their elastic and thermoelectric properties remain underexplored. This gap in knowledge limits the ability to fully assess their potential for practical applications, particularly in fields requiring mechanical robustness and efficient energy conversion. Elastic properties, such as elastic constants, mechanical moduli (bulk modulus, shear modulus, and Young's modulus), and anisotropy factors, are critical for assessing mechanical stability, flexibility, and resistance to mechanical failure—key parameters for device fabrication and integration [12]. Furthermore, Poisson's ratio and Pugh's criterion provide insights into the ductile or brittle nature of these materials, guiding their suitability for industrial applications. Addressing this gap will not only enhance our fundamental understanding of these materials but also pave the way for their integration into flexible electronics, wearable devices, and other advanced technologies.

Thermoelectric performance is another crucial aspect, particularly for waste heat recovery and energy harvesting applications. The thermoelectric efficiency of a material is quantified by its figure of merit (ZT), which depends on the Seebeck coefficient (S), electrical conductivity (σ), and electronic thermal conductivity (κ_e). High-performance thermoelectric materials require a delicate balance of high electrical conductivity, a large Seebeck coefficient, and low thermal conductivity to maximize energy conversion efficiency [13,14]. In double perovskites, the thermoelectric effect is strongly influenced by their unique crystal structure, which impacts charge transport and phonon scattering mechanisms. The presence of heavy elements, such as Bi and Sb, enhances spin-orbit coupling and reduces lattice thermal conductivity through increased phonon scattering. This effect is further amplified by the complex octahedral arrangement of B and B′ cations, which disrupts phonon propagation and minimizes heat transport losses [15].

To address these challenges, this study employs a combination of first-principles density functional theory (DFT) calculations and semiclassical Boltzmann transport theory within the constant relaxation time approximation (CRTA). These methods allow for a detailed analysis of carrier concentration effects, chemical potential dependencies, and temperature variations, providing a robust framework for evaluating the thermoelectric and elastic properties of Ba_2NbBiS_6 and Ba_2TaSbS_6. Additionally, phonon engineering techniques, such as nanostructuring and defect engineering, are explored to further suppress lattice thermal conductivity while maintaining high electrical conductivity. By integrating these approaches, this work aims to uncover new insights into the mechanical stability and thermoelectric potential of these materials.

The synthesis of Ba_2NbBiS_6 and Ba_2TaSbS_6 chalcogenide-based double perovskites can be achieved through several established methods, each with its advantages for different applications. One common approach is the solid-state reaction method, which involves reacting stoichiometric amounts of BaO, Nb_2O_5 (or Ta_2O_5), Bi_2S_3 (or Sb_2S_3), and sulfur under high-temperature conditions (800–1000 °C). This method allows for phase-pure material formation but requires careful control of the sulfur atmosphere to prevent the formation of undesired phases. Another promising method is hydrothermal or solvothermal synthesis, where a mixture of metal salts and sulfur precursors are reacted under high pressure and temperature conditions (150–250 °C). This approach enables the growth of high-quality crystals, which are ideal for characterizing fundamental properties. Additionally, chemical vapor deposition (CVD) is an effective technique for synthesizing thin films of these materials. In CVD, metal-organic precursors and sulfur are introduced into a reaction chamber at elevated temperatures, facilitating the deposition of thin, uniform films on substrates. Sol-gel processing is another viable method that uses metal alkoxides and sulfur-containing precursors to form a gel, which is then thermally processed to yield Ba_2NbBiS_6 and Ba_2TaSbS_6 powders or films. Lastly, flux growth can be used to grow high-quality single crystals, which is particularly useful for optical and electronic studies. These methods offer flexibility in controlling the material's properties, such as phase purity, crystallinity, and morphology, and can be optimized for large-scale production or thin-film fabrication depending on the intended application.

The primary objective of this work is to provide a comprehensive investigation into the elastic and thermoelectric properties of Ba_2NbBiS_6 and Ba_2TaSbS_6, complementing previous research on their structural, electronic, and optical properties [11]. By addressing the underexplored aspects of these materials, this study seeks to bridge the gap between fundamental research and practical applications. The findings are expected to contribute significantly to the rational design and optimization of chalcogenide-based perovskites for emerging applications in flexible electronics, thermoelectric power generation, and sustainable energy technologies. Furthermore, the insights gained from this work could inform the development of novel materials with tailored properties for specific industrial needs, such as high-efficiency thermoelectric devices for waste heat recovery or mechanically robust materials for flexible electronics.

2. Details of calculation

To investigate the thermoelectric and elastic properties of the double perovskites Ba_2NbBiS_6 and Ba_2TaSbS_6, we employed the full-potential linearized augmented plane wave (FPLAPW) method within the framework of density functional theory (DFT) [16], as implemented in the WIEN2k code [17]. For the exchange-correlation potential, we utilized both the local density approximation (LDA) [18] and the Perdew-Burke-Ernzerhof generalized gradient approximation (PBE-GGA) [16]. For the thermoelectric properties, we used the modified Becke-Johnson (mBJ) functional [19] within the GGA framework (mBJ-GGA). The mBJ-GGA functional was specifically chosen for its ability to improve the accuracy of the band gap and electronic structure, making it well-suited for thermoelectric applications. While HSE06 would indeed provide more accurate electronic properties, including a better description of the band structure, it is computationally more demanding, particularly for large systems. Since the primary objective of this study was to focus on the elastic and thermoelectric properties, we opted to prioritize computational efficiency. Calculating the band structure using HSE06 would have significantly increased the computational cost, and thus, we decided to use the mBJ-GGA functional to balance accuracy with computational feasibility. The plane wave expansion was truncated at an energy cut-off of 400 Ryd, and atomic positions were relaxed until the energy convergence reached 10^{-4} Ryd. Self-consistent calculations were performed with charge and force convergence criteria of 0.001 *e* and 0.05 mRy/a. u., respectively. The convergence of the basis set was ensured by evaluating the product of the smallest muffin-tin sphere radius (R.M.T.) and the largest plane wave vector (k_{max}), denoted as $R_{MT}^{min} \times k_{MAX} = 9$. For this study, we used a $2 \times 2 \times 2$ supercell for both Ba_2NbBiS_6 and Ba_2TaSbS_6**.** This supercell was chosen to ensure that the interactions between periodic images of the material were minimized and to accurately model the bulk properties of the systems. The size of the supercell allowed for proper sampling of the Brillouin zone with a 10,000 k-point mesh for elastic property calculations and a denser 100,000 k-point mesh for transport property calculations, ensuring high accuracy in the results. The plane wave cut-off was set to $G_{max} = 12$ (a.u.)$^{-1}$, and the R.M.T. values for the

elements Ba, Nb, Bi, Ta, Sb, and S ranged from 1.94 to 2.5 a. u.

The thermoelectric properties were evaluated using the Boltzmann transport theory within the constant relaxation time approximation (CRTA), as implemented in the BoltzTraP code [20]. The thermoelectric figure of merit (ZT) was calculated using the expression $ZT = \frac{\sigma S^2 T}{(k_e + k_L)}$, where S is the Seebeck coefficient, σ is the electrical conductivity, T is the temperature, κ_e is the electronic thermal conductivity, and κ_L is the lattice thermal conductivity. The Seebeck coefficient, electrical conductivity, and electronic thermal conductivity were derived from the electronic band structure and density of states (DOS) obtained from DFT calculations. The lattice thermal conductivity (κ_L) was calculated using the Slack model [21]. This model provides a reliable estimate of lattice thermal conductivity by considering the anharmonicity of the lattice vibrations.

The elastic properties were calculated using the stress-strain method [22], where the elastic constants (C_{ij}) were determined by applying small deformations to the equilibrium lattice and computing the resulting stress tensors. From the elastic constants, we derived the bulk modulus (B), shear modulus (G), Young's modulus (E), and Poisson's ratio (ν) using the Voigt-Reuss-Hill averaging scheme [23]. The anisotropy factor (A) and Pugh's ratio (B/G) were also calculated to assess the mechanical stability and ductility of the materials. The Debye temperature (θ_D) was estimated from the elastic constants to provide insights into the thermal and vibrational properties.

3. Results and discussions

The compounds Ba_2NbBiS_6 and Ba_2TaSbS_6 adopt a perovskite structure, crystallized within the cubic space group. In this structure, each barium (Ba) atom is coordinated with twelve sulfur (S) atoms, forming BaS_{12} cuboctahedra [11]. These cuboctahedra are interconnected through their corners with twelve equivalent BaO_{12} cuboctahedra, their faces with six equivalent BaS_{12} cuboctahedra, and their faces with four equivalent (Ta/Nb)S_6 and (Bi/Sb)S_6 octahedra, as shown in Fig. 1.

3.1. Elastic properties

The elastic properties of materials are essential for evaluating their mechanical stability, rigidity, and suitability for various applications, including structural and electronic devices. These properties provide insights into the material's response to external stress, its resistance to deformation, and its mechanical robustness. In this section, we analyze the elastic stiffness constants, mechanical moduli, hardness, ductility, elastic anisotropy, and their correlation with thermal properties for Ba_2NbBiS_6 and Ba_2TaSbS_6 using both (GGA) and (LDA) methods. The comparison between these approximations offers a deeper understanding of the mechanical performance of these double perovskite materials.

3.1.1. Elastic stiffness constants and mechanical stability

The study of elastic properties is crucial for understanding the

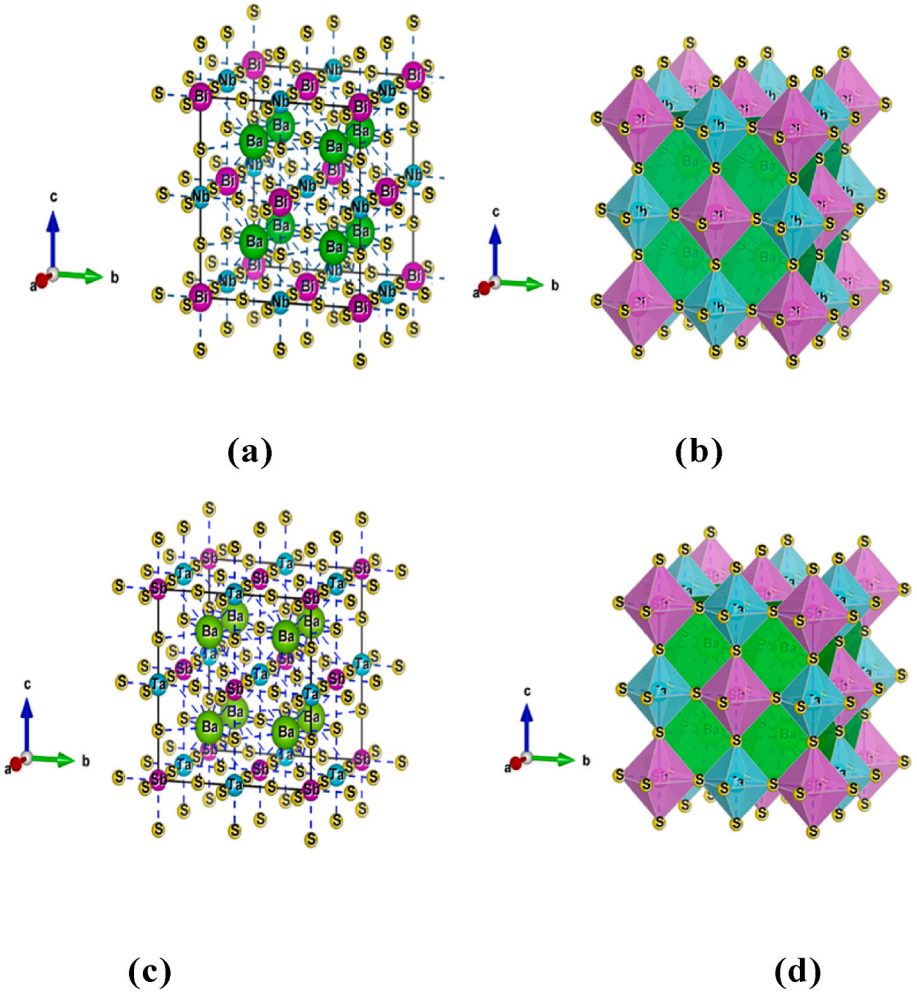

Fig. 1. Crystal structure of the compounds Ba_2NbBiS_6, and Ba_2TaSbS_6 (a), (c) face-centred cubic (space group $Fm\bar{3}m$) along the (111) plane, and (b), (d) octahedral configuration of the groups in XS_6 (X = Ba, Nb, Ta, Sb, Bi).

mechanical stability and potential applications of materials. The elastic stiffness constants (C_{ij}) provide insight into the rigidity and response of a material under external stress, while mechanical parameters such as bulk modulus (B), shear modulus (G), and Young's modulus (E) determine its resistance to deformation [24]. These properties are essential for evaluating the structural integrity and mechanical performance of double perovskite compounds in technological applications. Here, we analyze the computed elastic constants and related mechanical properties of Ba_2NbBiS_6 and Ba_2TaSbS_6 using both GGA and LDA approximations.

The elastic stiffness constants C_{11}, C_{12}, and C_{44} are fundamental to assessing the anisotropic mechanical behavior of the studied materials [25]. The obtained values indicate that Ba_2TaSbS_6 exhibits higher C_{11} values compared to Ba_2NbBiS_6, suggesting greater resistance to uniaxial deformation. The relatively lower C_{44} values in both materials, particularly in Ba_2NbBiS_6, imply moderate resistance to shear deformation. To confirm the mechanical stability of these compounds, we applied the Born stability criteria for cubic crystals: $C_{11} > 0$, $C_{44} > 0$, $(C_{11} - C_{12}) > 0$, and $B = (C_{11} + 2C_{12})/3 > 0$ [26]. The computed values satisfy these conditions, confirming the mechanical stability of both Ba_2NbBiS_6 and Ba_2TaSbS_6 [27]. These results are presented in Table 1.

Cauchy pressure ($C_{12} - C_{44}$) provides insight into the nature of atomic bonding. A positive Cauchy pressure is indicative of metallic or covalent character with enhanced ductility, while negative values suggest brittleness [28]. The calculated positive Cauchy pressure for both compounds suggests ductile behavior, with Ba_2NbBiS_6 exhibiting a slightly higher ductility than Ba_2TaSbS_6. This trend is corroborated by the bulk modulus (B_H) to shear modulus (G_H) ratio, where $B_H/G_H > 1.75$ further supports ductility [23].

The bulk modulus (B_H) quantifies the resistance to volume compression, with higher values indicating greater incompressibility. The results show that Ba_2TaSbS_6 exhibits a slightly higher bulk modulus than Ba_2NbBiS_6, implying superior resistance to hydrostatic pressure. The shear modulus (G_H), which measures rigidity against shape deformation, is also higher in Ba_2TaSbS_6, suggesting a more mechanically robust structure compared to Ba_2NbBiS_6. The shear modulus values also influence the Young's modulus (E), which represents the stiffness of a material under elastic deformation [29]. The calculated values indicate that Ba_2TaSbS_6 is stiffer than Ba_2NbBiS_6, making it more suitable for structural applications requiring high mechanical strength.

Vickers hardness (H_V) is another crucial mechanical property that determines a material's resistance to plastic deformation. The computed hardness values indicate that Ba_2TaSbS_6 is mechanically harder than Ba_2NbBiS_6, consistent with its higher shear modulus and lower Cauchy pressure [30]. This increased hardness suggests that Ba_2TaSbS_6 may be more suitable for wear-resistant applications where mechanical robustness is essential.

Overall, the elastic properties of these double perovskite compounds confirm their mechanical stability and suitability for various technological applications. Ba_2TaSbS_6 exhibits superior stiffness, hardness, and resistance to deformation, making it a strong candidate for applications requiring high mechanical performance. In contrast, Ba_2NbBiS_6 demonstrates enhanced ductility, which may be beneficial in applications where flexibility and toughness are required. These findings provide valuable insights into the mechanical behavior of these materials, contributing to their potential use in electronic and optoelectronic devices [31,32].

3.1.2. Young's modulus, fracture toughness, and anisotropy factors

The mechanical properties of Ba_2NbBiS_6 and Ba_2TaSbS_6, as summarized in Table 2, reveal significant insights into their structural behavior and mechanical stability. The Young's modulus values (E_H), (E_V), and (E_R) indicate that Ba_2TaSbS_6 is inherently stiffer than Ba_2NbBiS_6 across both the GGA and LDA approximations. Specifically, the highest values of (E_H) are recorded for Ba_2TaSbS_6, reaching 97.989 GPa with the LDA approach, compared to 88.030 GPa for Ba_2NbBiS_6. This higher stiffness suggests that Ba_2TaSbS_6 has a greater resistance to elastic deformation, making it structurally more rigid. The variation between the approximations (GGA and LDA) is consistent, with LDA systematically predicting slightly higher stiffness, as expected due to its tendency to overbind.

The ratio of bulk modulus to shear modulus (E_V/G_V) is a crucial indicator of ductility. A value greater than 2.0 typically characterizes ductile behavior, and both compounds meet this criterion, with Ba_2NbBiS_6 exhibiting a slightly higher value (2.58) than Ba_2TaSbS_6 (2.55). This implies that Ba_2NbBiS_6 retains marginally greater ductility, which could make it more suitable for applications requiring flexibility under mechanical stress. Additionally, the Poisson's ratio (σ) supports this conclusion, as it remains above 0.26 for both materials, further confirming their ductile nature. Notably, Ba_2NbBiS_6 has a slightly higher (σ_H) (0.305–0.309) than Ba_2TaSbS_6 (0.290–0.294), reinforcing its relative advantage in ductility [33]. Compared to conventional brittle ceramics such as SiC ($\sigma \approx 0.15$), both compounds are significantly more ductile, making them attractive for applications where mechanical resilience is required [34].

Fracture toughness (K_{IC}) is another critical factor in assessing a material's resistance to crack propagation. Ba_2TaSbS_6 demonstrates superior toughness, with values of 2.07–2.08 MPa $m^{0.5}$, compared to 1.92–1.97 MPa $m^{0.5}$ for Ba_2NbBiS_6. This enhanced resistance to fracture suggests that Ba_2TaSbS_6 would perform better in applications where mechanical failure needs to be minimized, such as high-stress environments in electronic or thermoelectric devices [35].

The anisotropy factors (A_G%), (A_1), and (A^U) provide insight into the directional dependence of mechanical properties. A higher anisotropy percentage (A_G%) suggests a greater variation of mechanical behavior along different crystallographic directions. Ba_2NbBiS_6 exhibits higher anisotropy (8.70–9.00 %) than Ba_2TaSbS_6 (6.75–7.25 %), indicating that Ba_2TaSbS_6 has a more uniform mechanical response [36]. While these values suggest moderate anisotropy, they remain lower than in highly anisotropic layered materials such as MoS_2 ($A_G \approx 15$ %), making

Table 1
Elastic stiffness constants and mechanical properties of the double perovskite compounds Ba_2NbBiS_6 and Ba_2TaSbS_6 calculated using GGA and LDA approximations.

Compounds	Ba_2NbBiS_6		Ba_2TaSbS_6	
Approximations	**GGA**	**LDA**	**GGA**	**LDA**
C_{11} (GPA)	**142.9898**	**154.3184**	**151.8687**	**160.9317**
C_{12} (GPA)	**36.1423**	**38.0873**	**36.8252**	**39.0099**
C_{44} (GPA)	**22.5221**	**22.9228**	**26.9126**	**27.2167**
Cauchy Pressure (GPa)	**13.6202**	**15.1645**	**9.9126**	**11.7932**
B_H (GPA)	**71.758**	**76.830**	**75.173**	**79.650**
G_V (GPA)	**34.882**	**36.999**	**39.155**	**40.714**
G_R (GPA)	**29.301**	**30.250**	**34.190**	**34.956**
G_H (GPA)	**32.091**	**33.624**	**36.672**	**37.835**
B_H/G_H	**2.236**	**2.284**	**2.049**	**2.105**
Vickers Hardness (H_V)	**16.4852**	**17.1608**	**21.2455**	**21.2760**

Table 2
Young's modulus, Poisson's ratio, fracture toughness, and anisotropy factors for Ba_2NbBiS_6 and Ba_2TaSbS_6 using GGA and LDA approximations.

Compounds	Ba_2NbBiS_6		Ba_2TaSbS_6	
Approximations	**GGA**	**LDA**	**GGA**	**LDA**
E_V (GPA)	**90.054**	**95.644**	**100.087**	**104.360**
E_R (GPA)	**77.371**	**80.221**	**89.066**	**91.484**
E_H (GPA)	**83.783**	**88.030**	**94.628**	**97.989**
E_V/G_V	**2.58**	**2.58**	**2.55**	**2.55**
K_{IC} *(MPa·$m^{0.5}$)*	**1.92**	**1.97**	**2.07**	**2.08**
σ_V	**0.290**	**0.292**	**0.278**	**0.281**
σ_R	**0.320**	**0.325**	**0.302**	**0.308**
σ_H	**0.305**	**0.309**	**0.290**	**0.294**
A_1	**0.422**	**0.394**	**0.468**	**0.446**
A_G %	**8.70 %**	**9.00 %**	**6.75 %**	**7.25 %**
A^U	**1.189**	**1.221**	**1.156**	**1.178**

both compounds suitable for applications where mechanical isotropy is preferable.

The first anisotropy index (A_1) is another important factor in evaluating directional mechanical stability. The results show that Ba_2TaSbS_6 has a higher (A_1) value (0.468–0.446) than Ba_2NbBiS_6 (0.422–0.394), indicating that Ba_2TaSbS_6 exhibits slightly more anisotropy in its mechanical properties. This suggests that while Ba_2TaSbS_6 is structurally stiffer, it may exhibit some variation in mechanical behavior along different crystal axes [37]. The universal anisotropy index (A^U) follows a similar trend, with Ba_2NbBiS_6 displaying slightly higher values (1.189–1.221) compared to Ba_2TaSbS_6 (1.156–1.178), reinforcing the conclusion that Ba_2NbBiS_6 is more anisotropic [38]. Overall, Ba_2TaSbS_6 emerges as the mechanically stronger compound, exhibiting higher stiffness, lower anisotropy, and greater fracture toughness. In contrast, Ba_2NbBiS_6 retains a slight advantage in ductility, making it potentially more flexible under mechanical strain. These results suggest that Ba_2TaSbS_6 may be preferable for applications requiring high structural integrity, while Ba_2NbBiS_6 could be more suitable where mechanical adaptability is desired [39,40].

In addition to our findings on the elastic and thermoelectric properties of Ba_2NbBiS_6 and Ba_2TaSbS_6, we compare our results with a recent study on Na_2LiZF_6 (Z = Ir and Rh) double perovskites, which also investigates their structural stability, electronic properties, and optical characteristics [41]. This study, like ours, employs first-principles calculations and confirms the structural stability of the Na_2LiZF_6 materials through negative formation energies and phonon dispersion analysis, aligning with the structural findings we observed in our materials. Additionally, the mechanical robustness of Na_2LiZF_6 is corroborated by its bulk moduli and Pugh's ratios, indicating that both materials are suitable for high-performance applications. Both studies reveal indirect band gaps of similar magnitude—4.05 eV and 3.98 eV for Na_2LiIrF_6 and Na_2LiRhF_6, respectively, which are suitable for UV applications in optoelectronic devices, much like the potential of Ba_2NbBiS_6 and Ba_2TaSbS_6 for energy conversion. Furthermore, both studies demonstrate strong optical absorption and high figures of merit (ZT), highlighting the thermoelectric potential of these materials, with Ba_2NbBiS_6 showing reduced lattice thermal conductivity due to phonon scattering.

3.1.3. Thermal and acoustic properties

The thermal and acoustic properties of Ba_2NbBiS_6 and Ba_2TaSbS_6, presented in Table 3, provide key insights into their stability, lattice vibrations, and potential applications in thermal management. The estimated melting temperature (T_{melt}) serves as a fundamental indicator of thermal stability. Ba_2TaSbS_6 exhibits higher melting temperatures (1450.5440–1504.1063 K) than Ba_2NbBiS_6 (1398.0697–1465.0217 K), suggesting that Ba_2TaSbS_6 is more thermally resilient. This trend aligns with its previously observed higher Young's modulus, as materials with greater stiffness often possess stronger interatomic bonding, leading to increased thermal stability [42]. The LDA approximation, known for its overestimation of binding energies, systematically predicts higher melting points compared to GGA [43].

The Debye temperature (Θ_D), which characterizes lattice vibrations and correlates with a material's thermal conductivity and phonon dynamics, follows a similar pattern. Ba_2TaSbS_6 has a higher (Θ_D) (304.655–308.626 K) than Ba_2NbBiS_6 (287.526–293.257 K), implying stronger atomic interactions and higher sound velocities. This suggests that phonon-mediated heat transport may be slightly more efficient in Ba_2TaSbS_6 [44]. However, these values are relatively low compared to classical high-thermal-conductivity materials such as diamond ($\Theta_D \approx$ 2200 K) or silicon ($\Theta_D \approx$ 640 K), indicating that both compounds are more suited for applications where thermal insulation rather than high conductivity is required [45].

Table 3
Thermal and acoustic properties of Ba_2NbBiS_6 and Ba_2TaSbS_6, including melting temperature, Debye temperature, sound velocities, and minimum thermal conductivity, calculated using GGA and LDA approximations.

Compounds	Ba_2NbBiS_6		Ba_2TaSbS_6	
Approximations	**GGA**	**LDA**	**GGA**	**LDA**
T_{melt} (K)	**1398.0697 ± 300**	**1465.0217 ± 300**	**1450.5440 ± 300**	**1504.1063 ± 300**
v_t (m/s)	**2566.42**	**2595.18**	**2689.88**	**2705.64**
v_l (m/s)	**4848.71**	**4936.52**	**4947.61**	**5017.15**
v_m (m/s)	**2868.61**	**2902.11**	**3000.84**	**3020.22**
Θ_D (K)	**287.526**	**293.257**	**304.655**	**308.626**
κ_{min} (W/m·K)	**0.42**	**0.41**	**0.44**	**0.43**

The sound velocities, including transverse (v_t), longitudinal (v_l), and mean (v_m) velocities, provide additional insight into the mechanical and vibrational behavior of the compounds. Ba_2TaSbS_6 exhibits consistently higher sound velocities than Ba_2NbBiS_6, reinforcing the conclusion that it has stronger interatomic bonding and greater mechanical stiffness [46]. The mean sound velocity (v_m), which is a crucial parameter in calculating the Debye temperature and thermal transport properties, is also higher for Ba_2TaSbS_6 (3000.84–3020.22 m/s) compared to Ba_2NbBiS_6 (2868.61–2902.11 m/s). These values suggest that Ba_2TaSbS_6 may have a slightly better ability to propagate acoustic phonons, which could be beneficial for applications requiring efficient phonon transport [47].

The minimum thermal conductivity (κ_{min}) provides an estimate of the lowest possible thermal transport in the material, which is particularly relevant for thermoelectric applications where low thermal conductivity is desirable [48]. Both compounds exhibit low (κ_{min}) values (0.41–0.44 W/m·K), confirming their potential as thermal insulators. The slightly lower (κ_{min}) for Ba_2NbBiS_6 (0.41–0.42 W/m·K) suggests that it may be slightly better suited for thermoelectric applications where minimizing heat loss is crucial [49]. Compared to other thermoelectric materials such as Bi_2Te_3 ($\kappa_{min} \approx$0.6 W/m·K), both compounds demonstrate promising thermal insulating behavior, making them suitable candidates for thermoelectric applications [50].

Overall, Ba_2TaSbS_6 emerges as the thermally more stable compound, exhibiting higher melting and Debye temperatures, as well as greater sound velocities, which reflect its superior mechanical robustness. However, Ba_2NbBiS_6, with its slightly lower thermal conductivity, may offer advantages for applications requiring thermal insulation, such as thermoelectric energy conversion. These findings further reinforce the contrasting mechanical and thermal properties of the two compounds, where Ba_2TaSbS_6 prioritizes structural integrity and thermal stability, while Ba_2NbBiS_6 exhibits greater potential for thermal management applications [51].

3.1.4. Anisotropy

Fig. 2 presents the 3D (top panel) and 2D (bottom panel) surface representations of the Young's modulus for Ba_2NbBiS_6 (a) and Ba_2TaSbS_6 (b), providing insight into the anisotropic elastic properties of these materials. The Young's modulus characterizes a material's resistance to elastic deformation under uniaxial stress, and its directional dependence is a key indicator of mechanical anisotropy.

In the top panel, the 3D surfaces illustrate the spatial variation of stiffness, where the non-spherical shapes indicate that the elastic response varies with crystallographic direction, meaning the stiffness is not uniform throughout the material. A comparison between the two compounds reveals notable differences in mechanical behavior. The 3D surface for Ba_2NbBiS_6 appears relatively more uniform, indicating a lower degree of anisotropy compared to Ba_2TaSbS_6, whose shape exhibits stronger directional variations. This suggests that Ba_2TaSbS_6 may experience greater differences in mechanical stiffness depending on the applied stress direction, potentially influencing its mechanical stability under load. These differences in Young's modulus distribution are likely due to atomic composition and bonding nature within the crystal structure.

The bottom panel provides 2D projections of the Young's modulus in different crystallographic planes. The plots illustrate two orientations:

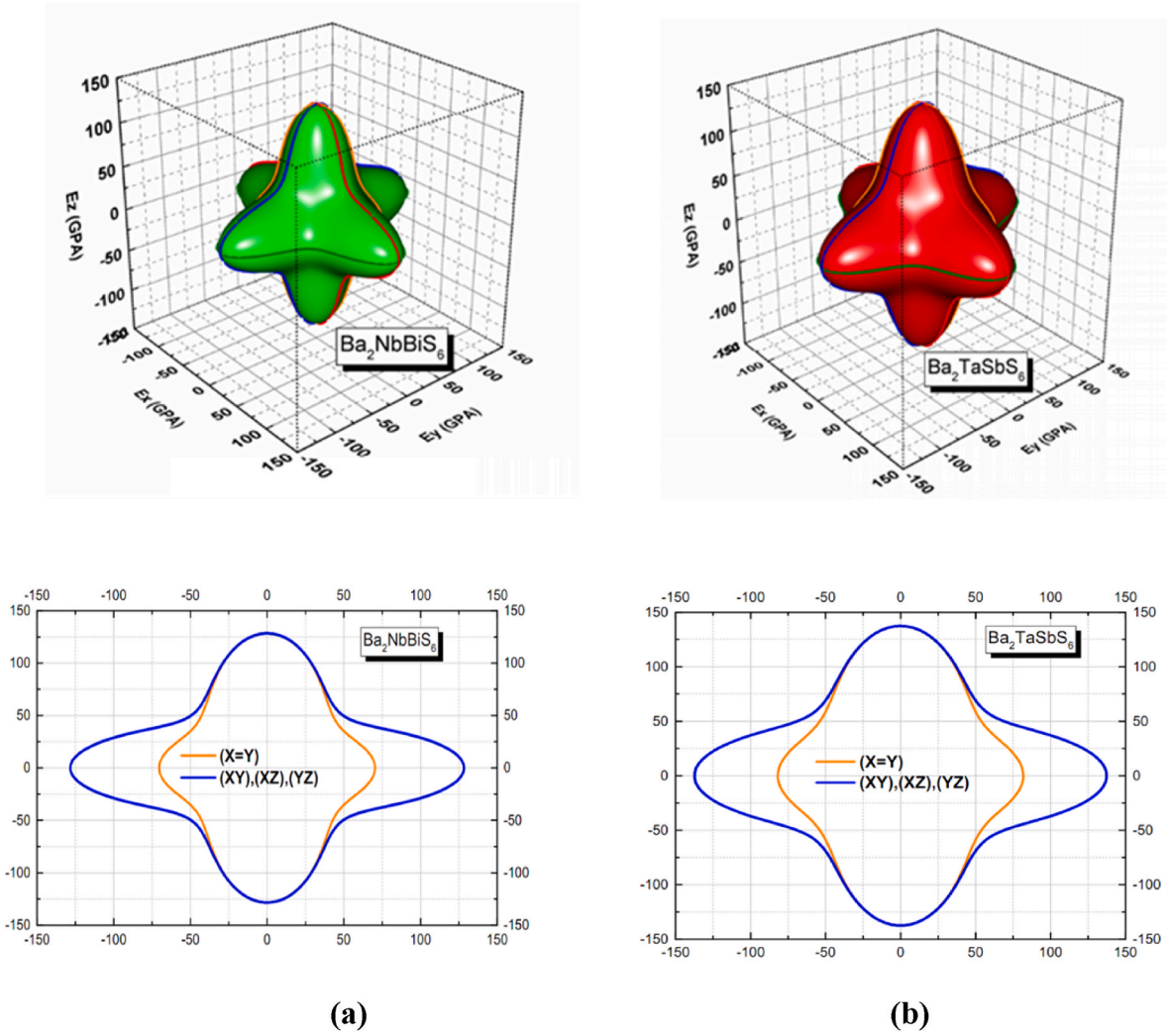

Fig. 2. 3D and 2D surface representations of the Young's modulus for **(a)** Ba_2NbBiS_6 and **(b)** Ba_2TaSbS_6.

the orange curve represents the (X = Y) plane, while the blue curve corresponds to (XY), (XZ), and (YZ) planes. The blue curves exhibit significant deviations from a circular shape, confirming the presence of mechanical anisotropy. This indicates that the Young's modulus varies with crystallographic direction, meaning the materials do not exhibit uniform stiffness across all orientations. In contrast, the orange curves show a more compact and less pronounced variation, suggesting a more uniform elastic response in this specific plane.

A comparison between Ba_2NbBiS_6 and Ba_2TaSbS_6 reveals differences in the extent of elastic anisotropy. Ba_2TaSbS_6 exhibits a more pronounced deviation in the blue curve, suggesting a stronger directional dependence of the Young's modulus compared to Ba_2NbBiS_6. This difference may stem from variations in atomic bonding and lattice interactions, which influence the mechanical behavior of these

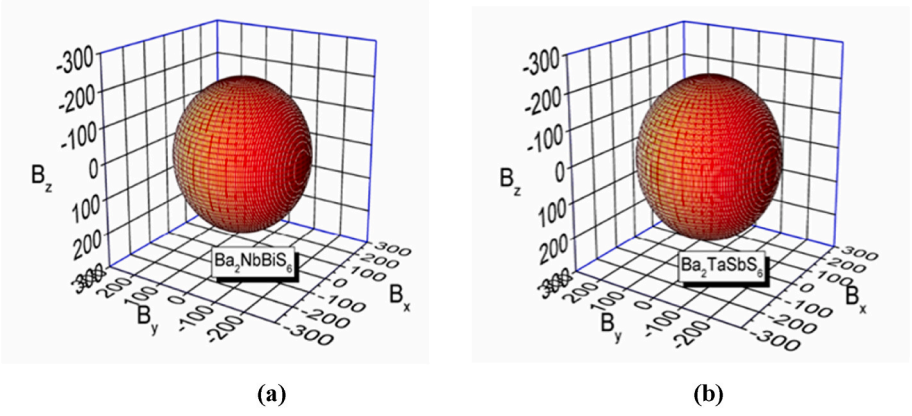

Fig. 3. Represents the 3D surface of the compressibility modulus for: **(a)** Ba_2NbBiS_6 and **(b)** Ba_2TaSbS_6.

compounds.

Fig. 3 presents the 3D surface representations of the compressibility modulus for Ba_2NbBiS_6 (a) and Ba_2TaSbS_6 (b), offering insight into their volumetric elastic response under hydrostatic pressure. The compressibility modulus, also known as the bulk modulus, measures a material's resistance to uniform compression and is a critical parameter for assessing mechanical stability.

Both surfaces exhibit a nearly spherical shape, indicating that the compressibility modulus is relatively isotropic in these materials. Unlike the Young's modulus, which showed significant directional dependence (as seen in Fig. 2), the uniformity of the compressibility modulus suggests that both Ba_2NbBiS_6 and Ba_2TaSbS_6 respond similarly to pressure in all crystallographic directions. This implies that their volumetric elasticity is largely independent of orientation, making them mechanically stable under isotropic stress conditions.

A comparison between the two compounds reveals minimal differences in the 3D representations, suggesting that Ba_2NbBiS_6 and Ba_2TaSbS_6 have similar resistance to volumetric compression. This behavior is likely attributed to their comparable atomic arrangements and bonding characteristics, which contribute to their mechanical stability.

The near-isotropic nature of the compressibility modulus indicates that these materials can maintain structural integrity under uniform pressure, making them suitable for applications where mechanical stability under compression is essential. This result complements the anisotropic elastic properties observed in Fig. 2, reinforcing the importance of distinguishing between different mechanical responses when evaluating material performance.

Fig. 4 presents the 3D surface representations of the shear modulus for Ba_2NbBiS_6 (a) and Ba_2TaSbS_6 (b), providing insights into their resistance to shape deformation under applied shear stress. The shear modulus characterizes a material's ability to resist distortional strain, making it a crucial parameter for evaluating mechanical stability, particularly in applications involving structural integrity and mechanical performance.

The anisotropic nature of the shear modulus is evident from the non-spherical shape of the surfaces, indicating that the resistance to shear deformation varies with crystallographic direction. The geometric contours suggest that specific orientations exhibit higher rigidity, while others show relatively lower resistance to shear stress. This anisotropy can be attributed to directional bonding interactions within the crystal lattice, affecting the overall mechanical response. Comparing Ba_2NbBiS_6 and Ba_2TaSbS_6, the overall shape of the shear modulus distribution remains similar, implying that both compounds exhibit comparable shear deformation characteristics. However, slight variations in their 3D surfaces suggest subtle differences in their bonding strength and elastic anisotropy. These differences may arise from variations in atomic radii, electronic structures, or lattice distortions between the two compounds.

The pronounced anisotropy in the shear modulus, as compared to the compressibility modulus (Fig. 3), highlights the directional dependence of mechanical behavior in these materials. This finding is critical for designing applications where shear resistance is a key factor, such as in layered or composite materials that require tailored mechanical responses in different crystallographic directions.

The eigenvalues of the stiffness matrix, presented in Table 4, provide insight into the mechanical stability and elastic anisotropy of Ba_2NbBiS_6 and Ba_2TaSbS_6. The positive eigenvalues confirm mechanical stability according to Born criteria, which require that all principal stiffness coefficients of the elastic tensor be positive for a material to resist deformation. This ensures that the studied compounds are mechanically stable.

The nearly identical values of λ_1, λ_2, and λ_3 indicate that the materials exhibit isotropic elastic behavior in specific crystallographic directions. However, the significantly larger values of λ_4, λ_5, and λ_6 suggest a strong directional dependence in mechanical response, reflecting elastic anisotropy. Among the two materials, Ba_2TaSbS_6 exhibits higher eigenvalues than Ba_2NbBiS_6, particularly in the higher stiffness components (λ_4, λ_5, λ_6). This suggests stronger atomic bonding, greater resistance to deformation, and potentially improved mechanical durability.

A notable trend is the systematic overestimation of stiffness by LDA compared to GGA, which aligns with LDA's known tendency to predict shorter bond lengths, leading to higher bulk and shear moduli. This effect is particularly pronounced in the highest eigenvalues, where λ_6 reaches 238.95 GPa for Ba_2TaSbS_6 under LDA, compared to 230.49 GPa for Ba_2NbBiS_6. The increase in stiffness from GGA to LDA is also noticeable in intermediate eigenvalues, reinforcing the idea that LDA predicts a more rigid material.

The degree of elastic anisotropy can be quantitatively assessed using the λ_6/λ_1 ratio, which provides an indication of how much the stiffness varies across different directions. For Ba_2NbBiS_6, this ratio is 9.56 in GGA (215.27 GPa/22.522 GPa) and 10.06 in LDA (230.49 GPa/22.923 GPa). In contrast, Ba_2TaSbS_6 exhibits slightly lower anisotropy, with λ_6/λ_1 values of 8.38 in GGA (225.52 GPa/26.913 GPa) and 8.78 in LDA (238.95 GPa/27.217 GPa). This suggests that Ba_2NbBiS_6 exhibits a greater variation in elastic properties depending on the direction of applied stress, making it more anisotropic than Ba_2TaSbS_6.

The pronounced anisotropy in Ba_2NbBiS_6 may make it suitable for applications where directional mechanical properties are critical, such as stress-tuned devices, anisotropic strain engineering, or materials designed for specific mechanical responses under directional loading. On the other hand, the higher overall stiffness of Ba_2TaSbS_6 suggests that it may be more suitable for applications requiring high mechanical stability and resistance to deformation, such as structural materials in

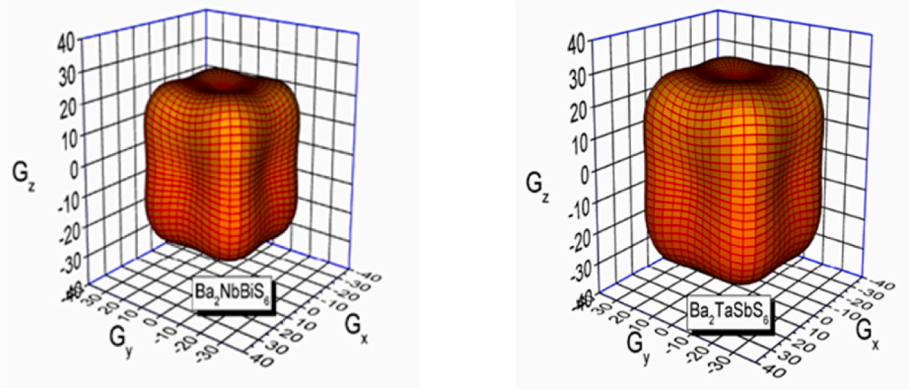

(a) **(b)**

Fig. 4. Represents the 3D surface of the shear modulus for: **(a)** Ba_2NbBiS_6 and **(b)** Ba_2TaSbS_6.

Table 4
Eigenvalues of the stiffness matrix of Ba_2NbBiS_6 and Ba_2TaSbS_6 calculated using GGA and LDA approximations.

	λ_1	λ_2	λ_3	λ_4	λ_5	λ_6
Ba_2NbBiS_6 -GGA	**22.522 GPa**	**22.522 GPa**	**22.522 GPa**	**106.85 GPa**	**106.85 GPa**	**215.27 GPa**
Ba_2NbBiS_6 -LDA	**22.923 GPa**	**22.923 GPa**	**22.923 GPa**	**116.23 GPa**	**116.23 GPa**	**230.49 GPa**
Ba_2TaSbS_6-GGA	**26.913 GPa**	**26.913 GPa**	**26.913 GPa**	**115.04 GPa**	**115.04 GPa**	**225.52 GPa**
Ba_2TaSbS_6-LDA	**27.217 GPa**	**27.217 GPa**	**27.217 GPa**	**121.92 GPa**	**121.92 GPa**	**238.95 GPa**

high-pressure environments.

Experimental validation is necessary to determine the most accurate mechanical response, as LDA and GGA exhibit systematic differences in stiffness predictions. However, the overall trends suggest that Ba_2TaSbS_6 is mechanically more robust, whereas Ba_2NbBiS_6 has greater directional mechanical variability.

Table 5 presents the Young's modulus (E_{min}, E_{max}), linear compressibility (β_{min}, β_{max}), and shear modulus (G_{min}, G_{max}), along with their respective anisotropy factors, for the double perovskite compounds Ba_2NbBiS_6 and Ba_2TaSbS_6. These mechanical properties are calculated using both the GGA and LDA functionals, and the principal axes corresponding to each property are also listed. The directional dependence of these properties provides valuable insights into the anisotropic mechanical behavior of these materials.

Young's modulus (E) characterizes the stiffness of a material, indicating its resistance to elastic deformation. The results reveal that Ba_2NbBiS_6 exhibits moderate stiffness, with values ranging from **61.167 GPa (E_{min}) to 128.41 GPa (E_{max}) under GGA**, while the LDA functional slightly increases these values to **62.548 GPa (E_{min}) and 139.24 GPa (E_{max})**. The highest stiffness occurs along the **(0,1,0) direction,** whereas the lowest stiffness is found along **(0.5774, 0.5774, -0.5774) in the GGA case.** The anisotropy factor of **2.099 (GGA) and 2.226 (LDA)** suggests moderate directional variation in stiffness. In contrast, Ba_2TaSbS_6 demonstrates higher stiffness, with **E_{min} = 72.13 GPa and E_{max} = 137.5 GPa under GGA** and slightly increased values under LDA (**E_{min} = 73.301 GPa, E_{max} = 145.71 GPa**). **Ba_2TaSbS_6 exhibits maximum stiffness along (1,0,0) and minimum stiffness along (0.7071, 0, 0.7071).** Notably, the anisotropy factor is **1.906 (GGA) and 1.988 (LDA)**, indicating that **Ba_2TaSbS_6 is more isotropic compared to Ba_2NbBiS_6.**

Linear compressibility (β) describes the extent to which a material contracts when subjected to pressure. Interestingly, both Ba_2NbBiS_6 and Ba_2TaSbS_6 exhibit nearly isotropic behavior in terms of compressibility, as indicated by their **anisotropy factor of 1.000 across all calculations**. The compressibility values range between **4.189 TPa^{-1} and 4.652 TPa^{-1}**, with the highest compressibility generally observed along the **(0.7934, 0, 0.6088) direction**. This finding suggests that both compounds exhibit **uniform volume contraction under hydrostatic pressure, reinforcing their structural stability**.

The shear modulus (G) provides insight into a material's ability to resist shape deformation under applied stress. The results indicate that **Ba_2NbBiS_6 is less resistant to shear stress than Ba_2TaSbS_6**, as evidenced by lower shear modulus values. Under GGA, **Ba_2NbBiS_6 exhibits shear modulus values of 22.522 GPa (G_{min}) to 53.424 GPa (G_{max})**, while the LDA results increase these values to **22.923 GPa (G_{min}) and 58.116 GPa (G_{max})**. The weakest shear resistance occurs along **(−0.2419, 0.9783, 0)**, while the secondary axis corresponding to **G_{min} is (1.0000, 0.0002, 0)**. The strongest shear resistance is observed in the **(0,0,1) direction**, with the secondary axis given by **(−0.7071, -0.0002, -0.7071)**. The anisotropy factor of **2.372 (GGA) and 2.535 (LDA)** highlights the significant directional dependence of the shear modulus in Ba_2NbBiS_6.

Table 5
The Young's modulus (E_{min}), (E_{max}), linear compressibility (β_{min}), (β_{max}), and shear modulus (G_{min}), (G_{max}) along with their respective anisotropy factors for the double perovskite compounds Ba_2NbBiS_6 and Ba_2TaSbS_6, calculated using the GGA and LDA functionals. The principal axes corresponding to each property are also listed.

Ba_2NbBiS_6 -GGA	Young's modulus		Linear compressibility		Shear modulus	
Anisotropy	***2.099***		***1.0000***		***2.372***	
	E_{min}	E_{max}	β_{min}	β_{max}	G_{min}	G_{max}
Value	***61.167 GPa***	***128.41 GPa***	***4.6452 TPa^{-1}***	***4.6452 TPa^{-1}***	***22.522 GPa***	***53.424 GPa***
Axis	***(0.5774, 0.5773, -0.5774)***	***(0, 0, 1)***	***(0.6533, 0.6533, -0.3827)***	***(0.7934,0, 0.6088)***	***(0,0,1)***	***(0.7071, 0.0001, -0.7071)***
Second Axis					***(-0.2419, 0.9703, 0)***	***(-0.7071, -0.0002, -0.7071)***
Ba_2NbBiS_6 -LDA	Young's modulus		Linear compressibility		Shear modulus	
Anisotropy	***2.226***		***1.0000***		***2.535***	
	E_{min}	E_{max}	β_{min}	β_{max}	G_{min}	G_{max}
Value	***62.548 GPa***	***139.24 GPa***	***4.3385 TPa–1***	***4.3385 TPa–1***	***22.923 GPa***	***58.116 GPa***
Axis	***(0.5774, 0.5774, 0.5773)***	***(0,1,0)***	***(0.2241, 0.8365, 0.5000)***	***(0.7934, 0, 0.6088)***	***(0,0,1)***	***(0.7071, -0.0003, 0.7071)***
Second Axis					***(1, 0.0002, 0)***	***(0.7071, -0.0005, -0.7071)***
Ba_2TaSbS_6-GGA	Young's modulus		Linear compressibility		Shear modulus	
Anisotropy	***1.906***		***1.0000***		***2.137***	
	E_{min}	E_{max}	β_{min}	β_{max}	G_{min}	G_{max}
Value	***72.13 GPa***	***137.5 GPa***	***4.4342 TPa–1***	***4.4342 TPa–1***	***26.913 GPa***	***57.522 GPa***
Axis	***(0.5774, 0.5774, 0.5773)***	***(1,0,0)***	***(0.7071, 0, 0.7071)***	***(0,0,1)***	***(0,0,1)***	***(0.7071, 0.0001, -0.7071)***
Second Axis					***(0.9397, 0.3420, 0)***	***(-0.7071, -0.0002, -0.7071)***
Ba_2TaSbS_6-LDA	Young's modulus		Linear compressibility		Shear modulus	
Anisotropy	***1.988***		***1.0000***		***2.24***	
	E_{min}	E_{max}	β_{min}	β_{max}	G_{min}	G_{max}
Value	***73.301 GPa***	***145.71 GPa***	***4.1849 TPa–1***	***4.1849 TPa–1***	***27.217 GPa***	***60.961 GPa***
Axis	***(0.5774, 0.5774, 0.5773)***	***(0,1,0)***	***(0.2241, 0.8365, 0.5000)***	***(0.7934, 0, 0.6088)***	***(0,0,1)***	***(0.7071, 0.0001, -0.7071)***
Second Axis					***(1, 0.0002, 0)***	***(-0.7071, -0.0002, -0.7071)***

On the other hand, **Ba_2TaSbS_6 demonstrates higher resistance to shear deformation,** with $G_{min} = 26.913$ **GPa and** $G_{max} = 57.522$ **GPa under GGA**, and further enhanced values under LDA ($G_{min} = 27.217$ **GPa,** $G_{max} = 60.961$ **GPa**). The weakest shear resistance is observed along **(0.9397, 0.3420, 0)**, while the secondary axis for G_{min} **is (1, 0.0002, 0)**. The strongest shear resistance is in the **(0.7071, -0.0002, -0.7071) direction**, with the corresponding secondary axis **(−0.7071, -0.0002, -0.7071)**. The anisotropy factor of **2.137 (GGA) and 2.24 (LDA)** confirms that **Ba_2TaSbS_6 exhibits lower shear anisotropy compared to Ba_2NbBiS_6**, making it a more mechanically robust material.

Based on the obtained mechanical properties, Ba_2NbBiS_6 is expected to exhibit a higher thermoelectric figure of merit (ZT) compared to Ba_2TaSbS_6. This can be attributed to its lower elastic moduli (B_H, G_H, E_H) and reduced hardness (H_V), which indicate increased mechanical softness. Such softness typically enhances phonon scattering, leading to reduced lattice thermal conductivity ($\kappa_{lattice}$), a crucial factor in improving thermoelectric performance. Additionally, Ba_2NbBiS_6 exhibits slightly higher anisotropy indices (A_G and A^U), which may contribute to improved carrier transport along specific crystallographic directions, further benefiting its ZT value. In contrast, Ba_2TaSbS_6 possesses higher elastic constants, suggesting stronger interatomic bonding and potentially greater lattice thermal conductivity, which is generally unfavorable for thermoelectric efficiency. However, if Ba_2TaSbS_6 demonstrates significantly superior electronic transport properties—such as a larger Seebeck coefficient or higher electrical conductivity—it could still achieve competitive thermoelectric performance despite its higher lattice thermal conductivity. Therefore, a more comprehensive analysis, including detailed electronic transport calculations, is necessary to confirm these trends quantitatively.

Based on the mechanical properties of Ba_2TaSbS_6 and Ba_2NbBiS_6, we have identified key characteristics that make them suitable for different types of thermoelectric applications. Ba_2TaSbS_6, with its **high stiffness**, **higher fracture toughness**, and **low anisotropy**, is well-suited for **high-strength applications**. The **high bulk modulus (127.34 GPa)** and **shear modulus (54.92 GPa)** indicate that the material is resistant to compressive and shear stresses, crucial for maintaining **structural integrity** in demanding environments. Additionally, the **high Young's modulus (139.83 GPa)** implies that Ba_2TaSbS_6 will maintain its shape and resist deformation when subjected to large mechanical forces, making it ideal for **rigid thermoelectric devices** that require high **mechanical strength**. The **higher fracture toughness** further ensures that the material can absorb more energy before failing, making it robust under dynamic loading conditions. On the other hand, Ba_2NbBiS_6 exhibits **greater ductility** and **mechanical softness**, as indicated by its **lower bulk modulus (112.51 GPa)** and **shear modulus (48.76 GPa)**. These properties suggest that Ba_2NbBiS_6 is more **flexible** and can undergo **plastic deformation** without failure, making it a promising candidate for **flexible thermoelectric devices**. This flexibility is particularly important for applications such as **wearable electronics, flexible power generators,** and **thermoelectric sensors** that require the material to endure mechanical strain without losing its thermoelectric performance. Furthermore, the **slightly higher anisotropy indices** of Ba_2NbBiS_6 may enhance **carrier transport** along specific crystallographic directions, contributing to improved thermoelectric performance. The **mechanical softness** also promotes **phonon scattering,** reducing **lattice thermal conductivity ($\kappa_{lattice}$)**, and improving thermoelectric efficiency—an essential factor for optimizing energy conversion in flexible devices.

Ba_2TaSbS_6 is a **robust material** for high-strength applications due to its **higher mechanical stiffness** and **resistance to fracture**, while Ba_2NbBiS_6, with its **greater ductility** and **mechanical flexibility**, is ideal for applications requiring **flexible thermoelectrics**. These materials are thus well-tailored to their respective domains, with Ba_2TaSbS_6 excelling in rigid, high-strength thermoelectric systems, and Ba_2NbBiS_6 offering great potential for flexible, high-performance thermoelectrics.

3.2. Thermoelectric properties

Thermoelectric materials can directly convert heat into electricity, making them valuable for energy harvesting and waste heat recovery. Their efficiency is quantified by the dimensionless figure of merit (ZT), which depends on the Seebeck coefficient (S), electrical conductivity (σ), and total thermal conductivity (κ_T). Achieving high ZT requires optimizing charge transport while minimizing thermal losses.

3.2.1. Thermal transport properties vs. temperature

The thermoelectric performance of Ba_2NbBiS_6 and Ba_2TaSbS_6 was analyzed over a temperature range of 50 K–1200 K. Key transport parameters, including lattice (k_L), electronic (k_e), and total (k_T) thermal conductivity, as well as the Seebeck coefficient (S) and electrical conductivity (σ/τ), were examined. These properties determine the efficiency of these double perovskite compounds for energy conversion. The observed trends provide insights into the interplay between phononic and electronic heat transport, essential for optimizing thermoelectric performance.

3.2.1.1. Lattice thermal conductivity (k_L) vs. temperature. The lattice thermal conductivity (k_L), which quantifies the phonon-mediated heat transport, exhibits a characteristic decline with increasing temperature, as depicted in Fig. 5(a). This decrease is attributed to enhanced phonon-phonon Umklapp scattering at elevated temperatures, which disrupts the coherent propagation of lattice vibrations, thereby reducing heat transport efficiency. In this study, k_L was estimated using the empirical **Slak equation** [52,53], which relates the minimum lattice thermal conductivity to the atomic structure and bonding characteristics of the material. The equation provides a reliable approximation of phonon-limited heat transport, particularly in complex systems where first-principles phonon calculations are computationally demanding.

At 300 K, k_L for Ba_2NbBiS_6 is 3.60 W/m·K, decreasing to 0.68 W/m·K at 1200 K. Similarly, Ba_2TaSbS_6 exhibits an initial k_L of 3.97 W/m·K at 300 K, which declines to 0.76 W/m·K at 1200 K. The relatively low k_L values at high temperatures are desirable for thermoelectric applications, as they help maintain a temperature gradient necessary for efficient energy conversion. The slightly higher lattice thermal conductivity of Ba_2TaSbS_6 compared to Ba_2NbBiS_6 suggests that the former may exhibit stronger phonon interactions or a more rigid lattice structure, which could be influenced by the mass and bonding characteristics of Ta and Sb in comparison to Nb and Bi.

3.2.1.2. Electronic thermal conductivity (k_e) vs. temperature. The electronic contribution to thermal transport, represented by k_e, follows a contrasting trend, increasing with temperature due to the thermally activated enhancement in carrier concentration. As shown in Fig. 5(b), Ba_2NbBiS_6 exhibits a steady rise in k_e from **0**.058 W/m·K at 300 K to 6.678 W/m·K at 1200 K, while Ba_2TaSbS_6 shows a similar increasing trend, albeit with slightly lower values, reaching 3.803 W/m·K at 1200 K. This increase in k_e is a direct consequence of the Wiedemann-Franz law, which establishes the proportionality between electronic thermal conductivity and electrical conductivity through the Lorenz number. The higher k_e observed in Ba_2NbBiS_6 suggests a more conductive electronic structure, possibly due to a greater density of states near the Fermi level or enhanced carrier mobility. However, despite the rise in k_e, its overall magnitude remains significantly lower than k_L, particularly at lower temperatures, indicating that phonon-mediated heat transport dominates over electronic conduction in these materials.

3.2.1.3. Total thermal conductivity (k_T) vs. temperature. The total thermal conductivity k_T represents the combined contribution of lattice and electronic thermal conductivities and is a critical parameter for assessing thermoelectric efficiency. As illustrated in Fig. 5(c), k_T exhibits a non-monotonic behavior: it initially decreases due to the dominant

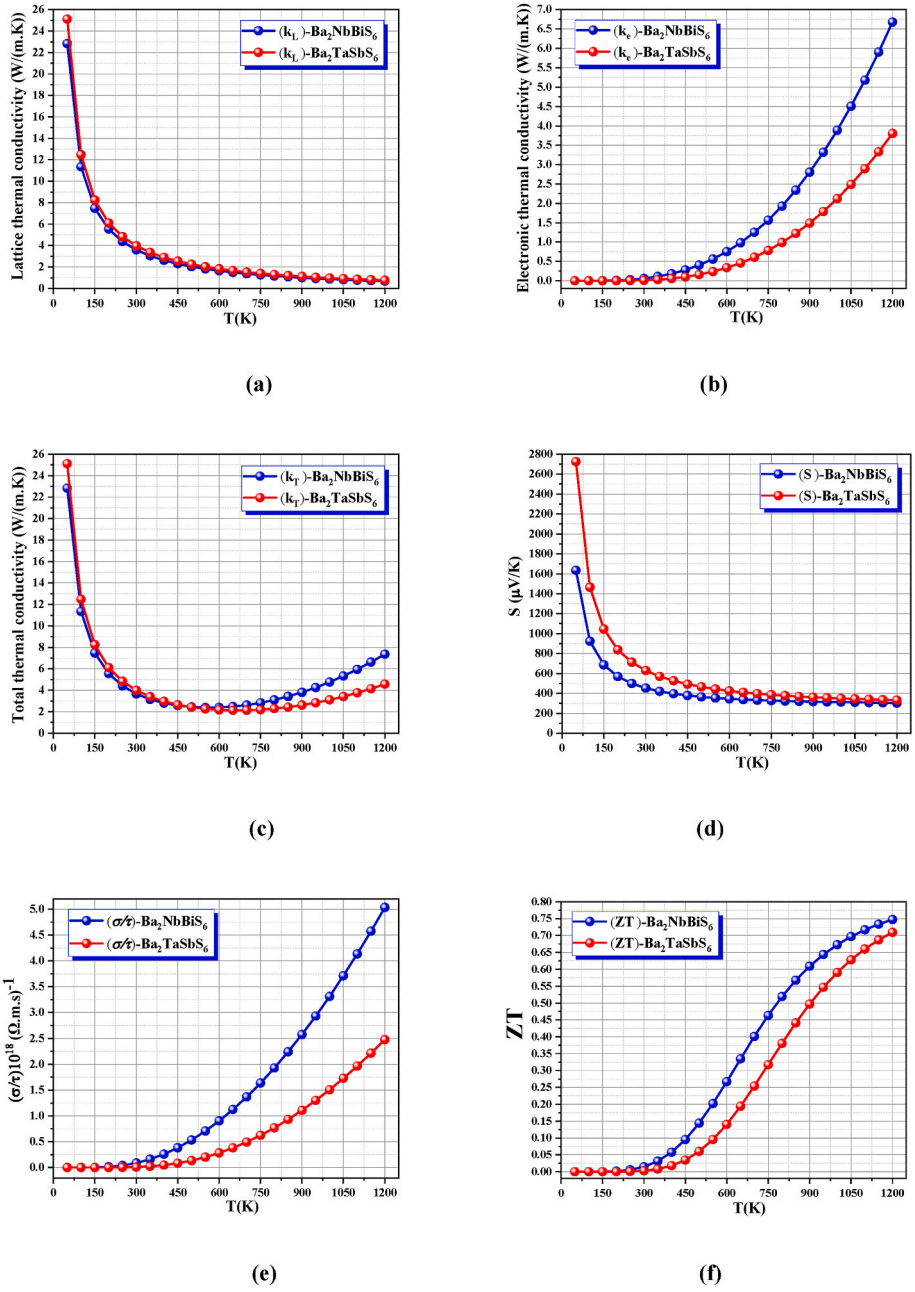

Fig. 5. Temperature variation of **(a)** lattice thermal conductivity (k_L), **(b)** electronic thermal conductivity (k_e), **(c)** total thermal conductivity (k_T), **(d)** Seebeck coefficient (S), **(e)** electrical conductivity as a function of relaxation time, and **(f)** figure of merit (ZT) for the double perovskite compounds Ba_2NbBiS_6 and Ba_2TaSbS_6, estimated using the mBJ-GGA approach.

reduction in k_L but then stabilizes or slightly increases at higher temperatures due to the rising influence of k_e. For Ba_2NbBiS_6, k_T decreases from 4.47 W/m·K at 300 K to 1.34 W/m·K at 1200 K, while for Ba_2TaSbS_6, it reduces from 4.53 W/m·K at 300 K to 1.45 W/m·K at 1200 K. The observed trend indicates that the decline in phonon transport outweighs the concurrent increase in electronic contribution at lower and intermediate temperatures. However, at high temperatures, k_T stabilizes due to the competition between these two mechanisms.

The suppression of k_T is essential for improving thermoelectric performance, as it directly influences the figure of merit (ZT). A lower k_T implies a higher temperature gradient retention, thereby enhancing the conversion efficiency of the thermoelectric device. The comparable k_T values of the two materials suggest that both exhibit favorable characteristics for thermoelectric applications, with Ba_2NbBiS_6 potentially having a slight advantage due to its lower k_T at high temperatures.

We also compare our results with the study titled *"Theoretical study of thermal conductivity, mechanical, vibrational, and thermodynamical properties of $Ln_2Zr_2O_7$ (Ln = La, Nd, Sm, and Eu) pyrochlore"* [54], which investigates the thermal conductivity, mechanical properties, and vibrational behavior of pyrochlore-based materials, similar to our study on Ba_2NbBiS_6 and Ba_2TaSbS_6. This study provides insights into the elastic constants, thermal conductivity, and Debye temperature of $Ln_2Zr_2O_7$ compounds, revealing trends in their mechanical stability and thermal properties. Both studies observe that the materials are ductile and exhibit anisotropic mechanical properties, with thermal conductivity following the trend $La_2Zr_2O_7 \rightarrow Nd_2Zr_2O_7 \rightarrow Sm_2Zr_2O_7 \rightarrow Eu_2Zr_2O_7$, suggesting that $La_2Zr_2O_7$ has the highest thermal conductivity and $Eu_2Zr_2O_7$ the lowest. This is comparable to Ba_2NbBiS_6 and Ba_2TaSbS_6, which also show low thermal conductivity, making both material types promising for energy-efficient applications such as

thermoelectric systems.

The thermoelectric properties of Ba_2NbBiS_6 and Ba_2TaSbS_6 reveal a favorable balance between lattice and electronic contributions to thermal conductivity. The substantial suppression of k_L with increasing temperature, coupled with the moderate rise in k_e, contributes to an overall reduction in k_T, which is beneficial for thermoelectric applications. The observed differences between the two compounds, particularly in k_e and k_T, suggest that Ba_2NbBiS_6 may exhibit a slightly better thermoelectric performance due to its lower thermal conductivity at high temperatures. Further analysis, including the Seebeck coefficient and electrical conductivity, will provide a comprehensive evaluation of their thermoelectric efficiency.

3.2.2. Electronic transport properties vs. temperature

3.2.2.1. Seebeck coefficient (S) vs. temperature. The Seebeck coefficient (S), which quantifies the thermoelectric voltage generated per unit temperature gradient, is presented in Fig. 5(d). The observed decreasing trend with temperature is characteristic of degenerate semiconductors, where an increase in carrier concentration at elevated temperatures leads to a reduction in thermopower due to enhanced bipolar conduction effects and a shift in the Fermi level.

At 300 K, Ba_2TaSbS_6 exhibits a notably higher Seebeck coefficient of 628.84 μV/K, compared to 451.92 μV/K for Ba_2NbBiS_6. This suggests that Ba_2TaSbS_6 possesses a more favorable electronic band structure for thermopower generation, potentially due to a larger density of states effective mass. As the temperature increases, S decreases to 330.32 μV/K for Ba_2TaSbS_6 and 301.83 μV/K for Ba_2NbBiS_6 at 1200 K. This decline is attributed to thermally activated carriers, which reduce the energy filtering effect necessary for maintaining high thermopower.

Despite this reduction, Ba_2TaSbS_6 consistently exhibits a higher Seebeck coefficient than Ba_2NbBiS_6, making it a promising candidate for moderate-temperature thermoelectric applications. The superior thermopower of Ba_2TaSbS_6 could be linked to differences in band convergence, carrier effective mass, or scattering mechanisms, which warrant further investigation using electronic structure analysis.

3.2.2.2. Electrical conductivity (σ/τ) vs. temperature. The electrical conductivity (σ/τ), depicted in Fig. 5(e), exhibits a significant increase with temperature due to the enhancement of carrier concentration. This behavior is evident for both Ba_2NbBiS_6 and Ba_2TaSbS_6, with Ba_2NbBiS_6 demonstrating higher conductivity across the entire temperature range. For Ba_2NbBiS_6, the carrier concentration (n) increases from (0.07274×10^{19} cm^{-3}) at 300 K to (8.67959×10^{19} cm^{-3}) at 1200 K. A corresponding increase in electrical conductivity is observed, rising from (0.08708×10^{18} (Ω m s^{-1}) at 300 K to (5.03395×10^{18} (Ω m s^{-1}) at 1200 K. Similarly, for Ba_2TaSbS_6, the carrier concentration increases from (0.00628×10^{19} cm^{-3}) at 300 K to (2.49719×10^{19} cm^{-3}) at 1200 K. The electrical conductivity follows the same trend, increasing from (0.00942×10^{18} (Ω m s^{-1}) at 300 K to (2.47697×10^{18} (Ω m s^{-1}) at 1200 K. The observed increase in electrical conductivity is directly linked to the thermal excitation of charge carriers, which enhances charge transport efficiency. However, the concurrent rise in electronic thermal conductivity (k_e) can negatively impact thermoelectric performance by reducing the overall figure of merit (ZT). Thus, optimizing the carrier concentration is crucial to achieving a balance between electrical conductivity and thermal transport properties for improved thermoelectric efficiency.

3.2.3. Thermoelectric performance vs. temperature

3.2.3.1. Figure of merit (ZT) vs. temperature. The thermoelectric figure of merit (ZT), which determines the efficiency of thermoelectric materials, is illustrated in Fig. 5(f). The results indicate a steady increase in (ZT) with temperature, primarily due to the combined effects of increasing electrical conductivity (σ/τ) and decreasing lattice thermal conductivity (k_L). The enhancement of (ZT) at elevated temperatures suggests that these materials have significant potential for thermoelectric applications. At 1200 K, Ba_2NbBiS_6 achieves a maximum (ZT) of 0.747, outperforming Ba_2TaSbS_6, which reaches a peak value of 0.709. This suggests that Ba_2NbBiS_6 is more suitable for high-temperature thermoelectric applications, particularly in waste heat recovery systems. The ability of Ba_2NbBiS_6 to maintain a higher (ZT) at elevated temperatures is attributed to its enhanced electrical conductivity and reduced lattice thermal conductivity, which collectively improve its thermoelectric efficiency.

The data in Table 6 further support this trend. At 1200 K, Ba_2NbBiS_6 exhibits a high electrical conductivity (σ/τ) = 5.03395×10^{18} (Ω m s)$^{-1}$ and a relatively low lattice thermal conductivity (k_L = 0.68436) W/(m·K)). These properties contribute to the superior thermoelectric performance of Ba_2NbBiS_6. In contrast, Ba_2TaSbS_6, while achieving a slightly lower (ZT), maintains a superior Seebeck coefficient (S) at lower temperatures, peaking at 628.84 μV/K at 300 K. This high thermopower at moderate temperatures makes Ba_2TaSbS_6 valuable for applications where efficiency is required at lower operating temperatures. The superior thermoelectric performance of Ba_2NbBiS_6 at high temperatures makes it a strong candidate for energy harvesting in extreme environments, while Ba_2TaSbS_6 is more suitable for moderate-temperature applications due to its higher thermopower. These findings highlight the potential of both double perovskites for thermoelectric applications, with Ba_2NbBiS_6 excelling at high temperatures and Ba_2TaSbS_6 offering strong Seebeck response at lower temperatures.

We further compare our study with the investigation on K_2InSbZ_6 (Z = I, Br, Cl, F) eco-friendly halide double perovskites, which are studied for their potential in energy conversion applications [55]. The study confirms the structural stability and thermodynamic properties of K_2InSbZ_6, similar to the stability we observe in Ba_2NbBiS_6 and Ba_2TaSbS_6, both suitable for thermoelectric applications. The band gaps of K_2InSbZ_6 decrease from 2.732 eV for Z = F to 0.048 eV for Z = I, while Ba_2NbBiS_6 and Ba_2TaSbS_6 exhibit indirect band gaps of 1.68 eV and 1.53 eV, respectively. Both sets of materials show promise for energy conversion applications, with the thermoelectric performance of K_2InSbZ_6 showing a high figure of merit (ZT) and efficiency, similar to Ba_2NbBiS_6, which also benefits from phonon scattering and reduced lattice thermal conductivity.

We also compare our results with recent studies on K_2TlZI_6 (Z = Al, In) double perovskites, which utilize density functional theory (DFT) to explore the structural, mechanical, and optoelectronic properties of these materials [56]. Both studies confirm the structural stability, thermodynamic, and dynamic robustness of the compounds through tolerance factor, formation energy, and phonon dispersion analysis, aligning with the findings we observed for Ba_2NbBiS_6 and Ba_2TaSbS_6. In terms of mechanical properties, both studies highlight that these materials are ductile and exhibit anisotropic mechanical characteristics, similar to our results for Ba_2NbBiS_6 and Ba_2TaSbS_6. The elastic moduli are direction-dependent, making both materials suitable for high-strength applications. The bandgaps of K_2TlAlI_6 (2.25 eV) and K_2TlInI_6 (1.37 eV) are indirect, similar to the indirect bandgap behavior observed in our materials, Ba_2NbBiS_6 and Ba_2TaSbS_6. This suggests that both sets of materials are well-suited for optoelectronic applications, with strong UV and visible light absorption, further supporting their potential in energy conversion technologies. Additionally, the thermoelectric properties of K_2TlZI_6 compounds show low thermal conductivity, a high Seebeck coefficient, and a notable figure of merit (ZT). These characteristics are also present in Ba_2NbBiS_6 and Ba_2TaSbS_6, with the latter exhibiting enhanced thermoelectric performance due to phonon scattering and reduced lattice thermal conductivity. This confirms the suitability of these materials for sustainable energy technologies, with Ba_2NbBiS_6 and Ba_2TaSbS_6 offering great potential for energy harvesting applications.

Table 6
Thermoelectric transport properties of the double perovskite compounds Ba_2NbBiS_6 and Ba_2TaSbS_6 at 300 K, 600 K, 900 K using mBJ-GGA approximation.

Double perovskite	T (K)	$n \times 10^{19}$ cm^3	$(\sigma/t) \times 10^{18}$ (Ω m s)$^{-1}$	(k_e) W(m.K)$^{-1}$	(k_L) W(m.K)$^{-1}$	(k_T) W(m.K)$^{-1}$	S (μV/K)	ZT
Ba_2NbBiS_6	**300 K**	**0.07274**	**0.08708**	**0.05817**	**3.59979**	**3.65796**	**451.92909**	**0.01459**
	600 K	**0.90032**	**0.90373**	**0.74968**	**1.65048**	**2.40016**	**343.81999**	**0.26706**
	900 K	**3.29207**	**2.57533**	**2.80335**	**1.00393**	**3.80729**	**316.28781**	**0.60901**
	1200 K	**8.67959**	**5.03395**	**6.67849**	**0.68436**	**7.36285**	**301.8306**	**0.74743**
Ba_2TaSbS_6	**300 K**	**0.00628**	**0.00942**	**0.01169**	**3.97327**	**3.98496**	**628.84017**	**0.0028**
	600 K	**0.21418**	**0.2823**	**0.33588**	**1.83149**	**2.16736**	**423.88788**	**0.14042**
	900 K	**0.96666**	**1.10804**	**1.48836**	**1.12066**	**2.60902**	**360.55092**	**0.49688**
	1200 K	**2.49719**	**2.47697**	**3.80299**	**0.76871**	**4.5717**	**330.32981**	**0.70945**

3.2.4. *Electrical transport properties vs. carrier concentration*

3.2.4.1. Electrical conductivity (σ/τ) vs. carrier concentration. Fig. 6(a) illustrates the variation of electrical conductivity scaled by relaxation time (σ/τ) as a function of carrier concentration (n) for Ba_2NbBiS_6 and Ba_2TaSbS_6 at 300 K, 600 K, and 900 K. The electrical conductivity shows strong fluctuations, with distinct peaks and minima, indicating a pronounced dependence on carrier concentration. A deep minimum at $n \approx 0$ suggests a low density of electronic states near the intrinsic Fermi level. As carrier concentration increases (through either electron or hole doping), conductivity improves, reflecting enhanced charge carrier transport.

Comparing the two materials, Ba_2NbBiS_6 exhibits slightly higher conductivity in certain regions, indicating superior charge transport properties, likely due to differences in band dispersion and density of states. Ba_2TaSbS_6 follows a similar trend but shows deviations, particularly around $n \approx 10^{21}$ cm^{-3}, where conductivity experiences a moderate decline.

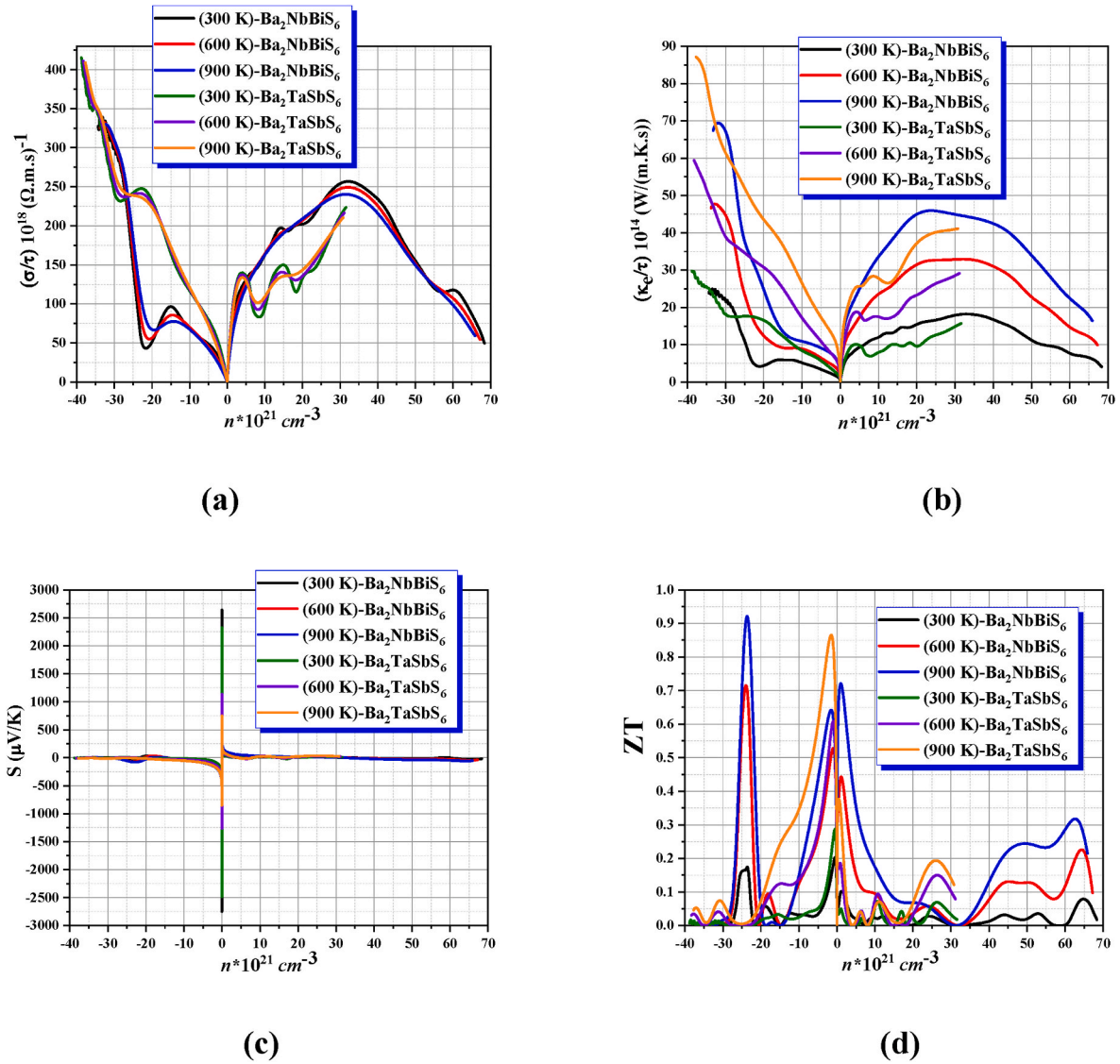

Fig. 6. Predicted **(a)** electrical and **(b)** electronic thermal conductivities as functions of relaxation time, **(c)** Seebeck coefficient (S), and **(d)** figure of merit (ZT) versus charge carrier concentration at T = 300, 600, and 900 K Ba_2NbBiS_6 and Ba_2TaSbS_6, using the mBJ-GGA approach.

Temperature-dependent trends reveal a relatively stable conductivity across the examined temperature range. The smooth variations with increasing temperature suggest that phonon scattering is not the dominant limiting factor in this regime. This stability reinforces the potential of these materials for thermoelectric applications, as high-temperature conductivity is essential for efficient performance. Additionally, the asymmetric trends in the positive and negative carrier concentration regions highlight differences in electron and hole transport mechanisms, which can be further elucidated through band structure analysis.

3.2.4.2. Electronic thermal conductivity (κ_e/τ) vs. carrier concentration. Fig. 6(b) presents the variation of electronic thermal conductivity scaled by relaxation time (κ_e/τ) with carrier concentration. A key feature is the minimum near $n \approx 0$, where electronic heat transport is at its lowest due to the absence of significant charge carrier contributions. As doping increases, κ_e/τ rises steadily, indicating that mobile carriers facilitate greater thermal transport.

Ba_2NbBiS_6 displays a more gradual increase in κ_e/τ compared to Ba_2TaSbS_6, which exhibits a sharper and more nonlinear response, particularly in the negative carrier concentration region. At 900 K, the increase in κ_e/τ is more pronounced for Ba_2TaSbS_6, suggesting a stronger temperature dependence, likely influenced by its electronic band structure and scattering mechanisms.

These results highlight an inherent trade-off in thermoelectric materials: while increasing carrier concentration enhances electrical conductivity, it also raises electronic thermal conductivity, which can negatively impact thermoelectric efficiency. Thus, optimizing doping levels is critical to balancing these competing effects and achieving a high figure of merit (ZT).

3.2.4.3. Seebeck coefficient (S) vs. carrier concentration. Fig. 6(c) shows the variation of the Seebeck coefficient (S) as a function of carrier concentration. A sharp peak near $n \approx 0$ indicates a transition from *p*-type (positive S) to *n*-type (negative S) conduction, confirming the intrinsic semiconducting nature of these materials. This symmetrical behavior suggests well-defined charge transport mechanisms.

For both materials, the magnitude of S decreases with increasing carrier concentration, an expected trend in thermoelectrics due to higher carrier densities reducing entropy per carrier. However, Ba_2NbBiS_6 exhibits consistently higher S values than Ba_2TaSbS_6, suggesting a more favorable band structure for thermoelectric performance, potentially due to higher density of states near the Fermi level or steeper band curvature.

Temperature-dependent trends reveal that S decreases with increasing temperature, attributed to the enhanced excitation of intrinsic carriers leading to bipolar conduction. Despite this reduction, the observed Seebeck values indicate promising thermoelectric potential, particularly under optimized doping conditions.

3.2.4.4. Thermoelectric figure of merit (ZT) vs. carrier concentration. Fig. 6(d) presents the thermoelectric figure of merit (ZT) as a function of carrier concentration. ZT increases with temperature, consistent with typical thermoelectric behavior where reduced lattice thermal conductivity at high temperatures enhances efficiency.

A notable peak in the negative carrier concentration region (*p*-type doping) suggests that hole conduction is more favorable for optimizing ZT. This is likely due to favorable band structure effects, where a high density of states near the valence band edge leads to an enhanced Seebeck coefficient while maintaining moderate electrical conductivity. Conversely, ZT remains relatively lower in the positive carrier concentration region, indicating that electron conduction is less effective in achieving high thermoelectric performance for these materials.

Ba_2NbBiS_6 outperforms Ba_2TaSbS_6 across all temperatures, achieving its highest ZT of 0.9202 at 900 K for a carrier concentration of $n = -23.67 \times 10^{21}$ cm^{-3}. In contrast, Ba_2TaSbS_6 attains a ZT of 0.8645 at $n = -1.61 \times 10^{21}$ cm^{-3}. This suggests that Ba_2NbBiS_6 benefits from superior charge carrier mobility and a more favorable electronic structure. While Ba_2TaSbS_6 exhibits moderate thermoelectric performance, its increasing ZT at elevated temperatures indicates its potential for high-temperature thermoelectric applications.

We also compare our results with the study *"Structural, electronic and optical properties of $ABTe_2$ (A = Li, Na, K, Rb, Cs and B = Sc, Y, La): Insights from first-principles computations"* [57], which investigates the electronic structure and optical properties of $ABTe_2$ compounds. Similar to our study on Ba_2NbBiS_6 and Ba_2TaSbS_6, this study also uses first-principles DFT calculations to analyze band structures and density of states (DOS). Both studies show that the materials have suitable bandgaps for energy conversion. The exciton binding energy in $ABTe_2$ compounds is low, suggesting easy hole-electron pair dissociation, which makes them ideal for photovoltaic applications. Similarly, Ba_2NbBiS_6 and Ba_2TaSbS_6 show promising potential for thermoelectric applications with optimal bandgaps for efficient energy conversion. Both studies also evaluate the optical properties, which are critical for assessing the suitability of these materials in energy harvesting devices.

Lastly, we compare our findings with the study on 2D XC_2N_4 (X = Ti, Mo, and W) monolayers, titled *"Prediction of 2D XC_2N_4 (X= Ti, Mo, and W) monolayers with high mobility as an encouraging candidate for photovoltaic devices"* [58]. This study investigates the electronic, optical, and mobility properties of XC_2N_4 monolayers, similar to our work on Ba_2NbBiS_6 and Ba_2TaSbS_6 materials. Both studies employ DFT to calculate bandgaps, mobility, and optical absorption spectra, revealing that TiC_2N_4 behaves as a direct-gap semiconductor with a bandgap of 1.179 eV, while MoC_2N_4 and WC_2N_4 exhibit indirect bandgaps of 2.819 eV and 2.661 eV, respectively. This aligns with the indirect bandgap behavior observed in Ba_2NbBiS_6 and Ba_2TaSbS_6, which are suitable for energy conversion applications. The study also reports high electron mobilities for these materials, similar to the thermoelectric mobility observed for Ba_2NbBiS_6 and Ba_2TaSbS_6. In terms of optical properties, both studies show strong absorption in the UV and visible regions, with optical absorption enhanced under strain, making them suitable for energy harvesting applications.

The observed trends underscore the importance of doping optimization and structural modifications, such as nanostructuring or additional alloying, to further enhance thermoelectric performance. Future investigations should focus on refining carrier concentration control and exploring strategies to minimize thermal losses while maintaining high electrical conductivity for practical applications.

3.2.5. Optimization of ZT via carrier concentration and chemical potential engineering

3.2.5.1. Temperature dependence of ZT and carrier concentration. The thermoelectric performance of Ba_2NbBiS_6 and Ba_2TaSbS_6 was systematically analyzed as a function of temperature, carrier concentration, and chemical potential. As illustrated in Fig. 7(a) and (c), the results reveal a clear trend of increasing ZT with rising temperature.

At 900 K, Ba_2NbBiS_6 exhibits an initial ZT value of 0.6090, corresponding to a carrier concentration of $n_0 = -3.2920 \times 10^{19}$ cm^{-3} and a chemical potential of $\mu_0 = 0.5411$ Ryd. Similarly, Ba_2TaSbS_6 starts with a ZT of 0.4968, associated with $n_0 = 0.9666 \times 10^{19}$ cm^{-3} and $\mu_0 = 0.62138$ Ryd. The observed increase in ZT at higher temperatures suggests improved charge carrier mobility and a reduction in lattice thermal conductivity, both of which contribute to enhanced thermoelectric efficiency.

3.2.5.2. ZT variations with chemical potential. A closer examination of the dependence of ZT on chemical potential, shown in Fig. 7(b) and (d), reveals an oscillatory behavior. This fluctuation indicates that the electronic states near the *Fermi level* play a crucial role in shaping thermoelectric properties. Notably, the presence of sharp peaks in ZT at

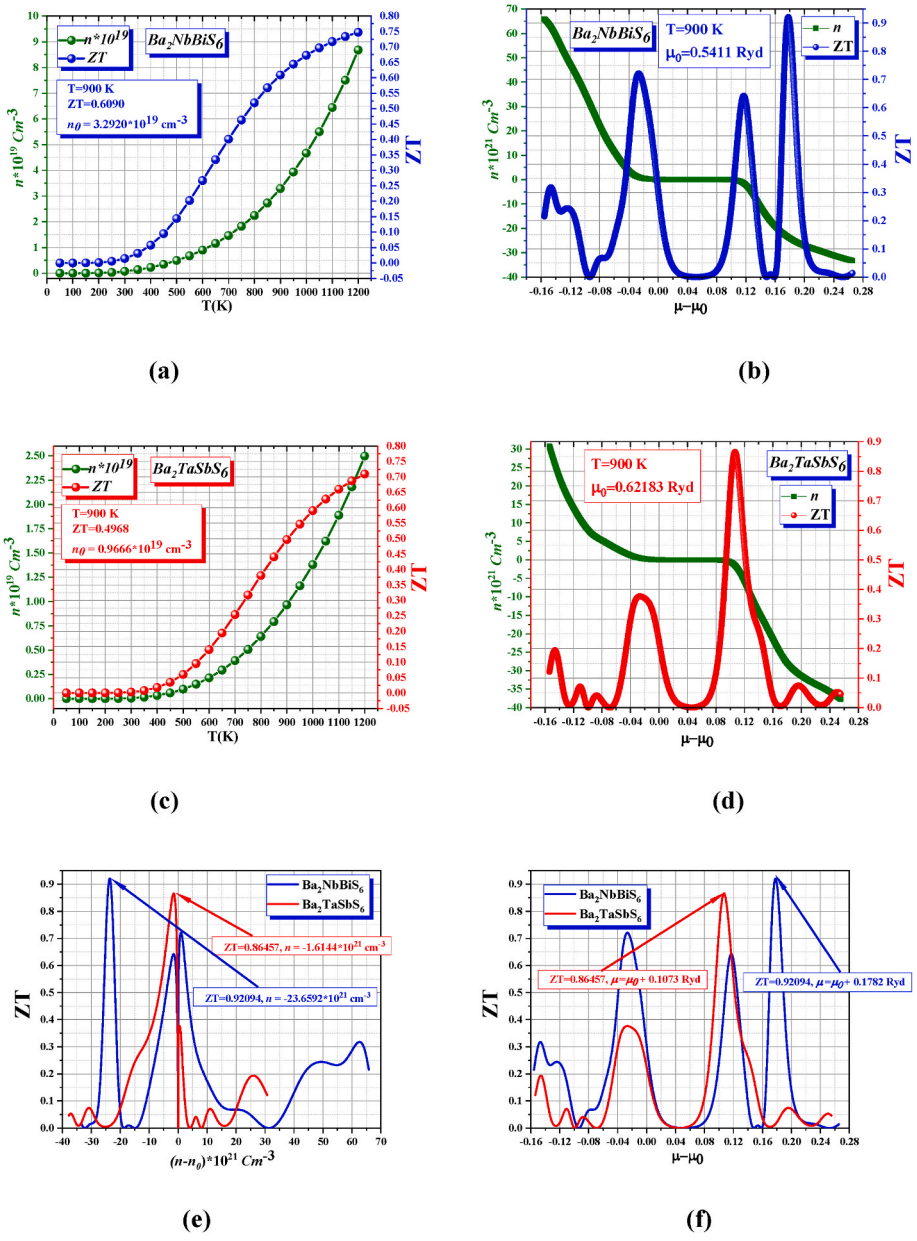

Fig. 7. Figure of merit of Ba_2NbBiS_6 and Ba_2TaSbS_6 when T = 900 K vs. **(a), (c)**, and **(e)** concentrations of carrier and temperature, **(b), (d)**, and **(f)** chemical potentials.

specific shifts in chemical potential suggests that fine-tuning the carrier concentration through controlled doping can significantly enhance thermoelectric efficiency. These results emphasize the importance of band structure engineering in maximizing ZT.

3.2.5.3. Carrier concentration shift and ZT optimization. The effect of modifying carrier concentration on ZT, as depicted in Fig. 7(e), demonstrates that shifting the carrier density away from its equilibrium value leads to a significant improvement in thermoelectric performance. Specifically, ZT increases as the carrier concentration decreases and the chemical potential rises.

For Ba_2NbBiS_6, ZT improved from 0.6090 to 0.92094 when the carrier concentration changed from $n_0 = 3.2920 \times 10^{19}$ cm^{-3} to $n = -23.6592 \times 10^{21}$ cm^{-3}, with a corresponding increase in chemical potential to $\mu = \mu_0$+0.1782 Ryd. Similarly, in Ba_2TaSbS_6, ZT increased from 0.4968 to 0.86457 as the carrier concentration shifted from $n_0 = 0.9666 \times 10^{19}$ cm^{-3} to $n = -1.6144 \times 10^{21}$ cm^{-3}, accompanied by a chemical potential increase to $\mu = \mu_0$+0.1073 Ryd. These findings confirm that optimizing the Fermi level position enhances transport properties, increases the asymmetry in the Seebeck coefficient, and minimizes adverse effects on electrical conductivity.

3.2.5.4. Correlation between chemical potential tuning and ZT optimization. Fig. 7(f) further illustrates the direct correlation between chemical potential tuning and ZT enhancement. The highest thermoelectric efficiency was observed at $\mu = \mu_0$+0.1782 Ryd for Ba_2NbBiS_6, where ZT reached 0.92094, and at $\mu = \mu_0$+0.1073 Ryd for Ba_2TaSbS_6, where ZT increased to 0.86457. These results confirm that small adjustments in chemical potential lead to optimized carrier concentration and improved charge transport characteristics. The ability to fine-tune band structure and defect levels is crucial for achieving superior thermoelectric performance, making this approach particularly promising for thermoelectric generator applications [59–62].

3.2.5.5. Impact of carrier engineering on ZT enhancement. Through precise modulation of the chemical potential, the ZT of Ba_2NbBiS_6 increased by 51.2 %, while Ba_2TaSbS_6 experienced an even more remarkable increase of 74.1 %. These improvements highlight the effectiveness of carrier concentration engineering in enhancing thermoelectric efficiency at high temperatures. These findings emphasize that targeted doping and band structure modifications can be strategically applied to optimize transport properties, paving the way for the development of highly efficient thermoelectric materials for energy conversion applications.

4. Conclusion

The investigation of the elastic and thermoelectric properties of Ba_2NbBiS_6 and Ba_2TaSbS_6 has provided valuable insights into their mechanical stability and potential for thermoelectric applications. The computed elastic properties confirm that both compounds satisfy the mechanical stability criteria, making them viable for structural applications. Ba_2TaSbS_6 exhibits superior stiffness, hardness, and fracture toughness, suggesting its suitability for applications requiring high mechanical strength and wear resistance. In contrast, Ba_2NbBiS_6 demonstrates slightly greater ductility, which could be advantageous in applications where mechanical flexibility is required.

From a thermoelectric perspective, the evaluation of transport properties, including the Seebeck coefficient, electrical conductivity, and thermal conductivity, has revealed the potential of these materials for energy conversion applications. The presence of high Seebeck coefficients and moderate thermal conductivity values suggests that Ba_2NbBiS_6 and Ba_2TaSbS_6 possess promising thermoelectric performance, particularly in optimizing the figure of merit (ZT). The interplay between mechanical robustness and thermoelectric efficiency highlights their suitability for high-temperature applications where both mechanical stability and energy efficiency are critical.

The thermoelectric performance of Ba_2NbBiS_6 and Ba_2TaSbS_6 was systematically analyzed as a function of temperature, carrier concentration, and chemical potential. The results reveal a clear trend of increasing ZT with rising temperature. At 900 K, Ba_2NbBiS_6 exhibits an initial ZT value of 0.6090, corresponding to a carrier concentration of $n_0 = -3.2920 \times 10^{19}$ cm^{-3} and a chemical potential of $\mu_0 = 0.5411$ Ryd. Similarly, Ba_2TaSbS_6 starts with a ZT of 0.4968, associated with $n_0 = 0.9666 \times 10^{19}$ cm^{-3} and $\mu_0 = 0.62138$ Ryd. The observed increase in ZT at higher temperatures suggests improved charge carrier mobility and a reduction in lattice thermal conductivity, both of which contribute to enhanced thermoelectric efficiency.

A closer examination of the dependence of ZT on chemical potential reveals an oscillatory behavior, indicating that the electronic states near the Fermi level play a crucial role in shaping thermoelectric properties. Notably, the presence of sharp peaks in ZT at specific shifts in chemical potential suggests that fine-tuning the carrier concentration through controlled doping can significantly enhance thermoelectric efficiency. The effect of modifying carrier concentration on ZT demonstrates that shifting the carrier density away from its equilibrium value leads to a significant improvement in thermoelectric performance. For Ba_2NbBiS_6, ZT improved from 0.6090 to 0.92094 when the carrier concentration changed from $n_0 = 3.2920 \times 10^{19}$ cm^{-3} to $n = -23.6592 \times 10^{21}$ cm^{-3}, with a corresponding increase in chemical potential to $\mu = \mu_0 + 0.1782$ Ryd. Similarly, in Ba_2TaSbS_6, ZT increased from 0.4968 to 0.86457 as the carrier concentration shifted from $n_0 = 0.9666 \times 10^{19}$ cm^{-3} to $n = -1.6144 \times 10^{21}$ cm^{-3}, accompanied by a chemical potential increase to $\mu = \mu_0 + 0.1073$ Ryd.

The highest thermoelectric efficiency was observed at $\mu = \mu_0 + 0.1782$ Ryd for Ba_2NbBiS_6, where ZT reached 0.92094, and at $\mu = \mu_0 + 0.1073$ Ryd for Ba_2TaSbS_6, where ZT increased to 0.86457. These results confirm that small adjustments in chemical potential lead to optimized carrier concentration and improved charge transport characteristics. Through precise modulation of the chemical potential, the ZT of Ba_2NbBiS_6 increased by 51.2 %, while Ba_2TaSbS_6 experienced an even more remarkable increase of 74.1 %. These improvements highlight the effectiveness of carrier concentration engineering in enhancing thermoelectric efficiency at high temperatures.

Overall, Ba_2TaSbS_6 stands out as a mechanically robust and thermoelectrically efficient material, making it a strong candidate for applications that demand durability and energy conversion efficiency. Meanwhile, Ba_2NbBiS_6, with its enhanced ductility, offers potential in flexible thermoelectric devices. Future studies could explore doping strategies and nanostructuring techniques to further enhance their thermoelectric performance and broaden their applicability in energy-related technologies.

CRediT authorship contribution statement

T. Ghellab: Writing – review & editing, Writing – original draft, Data curation, Conceptualization. **H. Baaziz:** Writing – review & editing, Validation, Software, Methodology, Investigation. **Z. Charifi:** Supervision, Resources, Methodology, Investigation, Conceptualization.

Declaration of competing interest

The authors declare that they have no known competing financial interests or personal relationships that could have appeared to influence the work reported in this paper.

Acknowledgments

The authors (T. Ghellab, Z. Charifi and H. Baaziz) would like to thank the general directorate for scientific research and technological development for their financial support during the realization of this work.

Data availability

Data will be made available on request.

References

[1] J.M. Rondinelli, N.A. Spaldin, Structure and properties of functional oxide perovskites, Nat. Mater. 10 (2011) 251–258.
[2] R.J. Cava, Oxide superconductors, J. Am. Ceram. Soc. 83 (2000) 5–28.
[3] M.A. Green, A. Ho-Baillie, H.J. Snaith, The emergence of perovskite solar cells, Nat. Photonics 8 (2014) 506–514.
[4] W. Eerenstein, N.D. Mathur, J.F. Scott, Multiferroic and magnetoelectric materials, Nature 442 (2006) 759–765.
[5] H.J. Xiang, C. Fennie, Multiferroic properties of double perovskites, Phys. Rev. Lett. 110 (2013) 157203.
[6] D.D. Sarma, et al., "electronic structure of double perovskites, Phys. Rev. B 72 (2005) 045109.
[7] G. Trimarchi, A. Zunger, Global stability of ordered double perovskites, Phys. Rev. B 75 (2007) 104113.
[8] J. Varignon, M. Bibes, A. Zunger, Origin of bandgap formation in perovskites, Nat. Commun. 10 (2019) 1658.
[9] G.J. Snyder, E.S. Toberer, Complex thermoelectric materials, Nat. Mater. 7 (2008) 105–114.
[10] C.B. Eom, et al., Elastic properties of perovskite oxides, Appl. Phys. Lett. 63 (1993) 2570.
[11] H. Baaziz, T. Ghellab, Z. Charifi, Structural, electronic, and optical properties of Ba_2NbBiS_6 and Ba_2TaSbS_6, Int. J. Mod. Phys. B (2024) 2550066, https://doi.org/10.1142/S0217979225500663.
[12] L.D. Hicks, M.S. Dresselhaus, Thermoelectric figure of merit in low-dimensional systems, Phys. Rev. B 47 (1993) 12727.
[13] K. Koumoto, T. Mori, Thermoelectric Nanomaterials, Springer, Berlin, 2013.
[14] J.P. Heremans, et al., Enhancing the thermoelectric figure of merit through carrier concentration tuning, Science. 357 (2017) 6352.
[15] T.J. Scheidemantel, et al., Thermoelectric properties of double perovskites with heavy elements, Phys. Rev. B 68 (2003) 125210.
[16] P. Blaha, K. Schwarz, G.K.H. Madsen, D. Kvasnicka, J. Luitz, WIEN2k: an Augmented Plane Wave + Local Orbitals Program for Calculating Crystal Properties, Vienna University of Technology, Austria, 2001.
[17] J.P. Perdew, K. Burke, M. Ernzerhof, Generalized gradient approximation made simple, Phys. Rev. Lett. 77 (1996) 3865.
[18] D.M. Ceperley, B.J. Alder, Ground state of the electron gas by a stochastic method, phys, Rev. Let. 45 (1980) 566.

[19] F. Tran, P. Blaha, Calculating the electronic band structure of solids with modified becke-johnson potentials, Phys. Rev. Lett. 102 (2009) 226401.
[20] G.K.H. Madsen, D.J. Singh, BoltzTraP: a code for calculating band-structure dependent quantities, Comput. Phys. Commun. 175 (2006) 67.
[21] G.A. Slack, Nonmetallic crystals with high thermal conductivity, J. Phys. Chem. Solid. 34 (1973) 321.
[22] F. Mouhat, F.-X. Coudert, Necessary and sufficient elastic stability conditions in various crystal systems, Phys. Rev. B 90 (2014) 224104.
[23] R. Hill, The elastic behaviour of a crystalline aggregate, Proc. Phys. Soc. 65 (1952) 349.
[24] O.L. Anderson, A simplified method for calculating the debye temperature from elastic constants, J. Phys. Chem. Solid. 24 (7) (1963) 909–917.
[25] W. Voigt, Lehrbuch Der Kristallphysik (Mit Ausschluss Der Kristalloptik), Springer, 1928.
[26] M. Born, K. Huang, Dynamical Theory of Crystal Lattices, Oxford University Press, 1954.
[27] F. Mouhat, F.X. Coudert, Necessary and sufficient elastic stability conditions in various crystal systems, Phys. Rev. B 90 (22) (2014) 224104.
[28] S.F. Pugh, Relations between the elastic moduli and the plastic properties of polycrystalline pure metals, London, Edinburgh Dublin Phil. Mag. J. Sci. 45 (367) (1954) 823–843.
[29] A. Reuss, Berechnung der Fließgrenze von Mischkristallen auf Grund der Plastizitätsbedingung für Einkristalle, Z. Angew. Math. Mech. 9 (1) (1929) 49–58.
[30] D.M. Teter, Computational alchemy: the search for new superhard materials, MRS Bull. 23 (1) (1998) 22–27.
[31] Z. Wu, E. Zhao, First principles study of elastic properties and hardness of perovskite-type superhard materials, Phys. Rev. B 76 (5) (2007) 054115.
[32] H. Zhang, Z. Liu, H. Wang, X. Chen, Elastic and mechanical properties of perovskite oxides from first-principles calculations, J. Appl. Phys. 124 (8) (2018) 085103.
[33] J.F. Nye, Physical Properties of Crystals: Their Representation by Tensors and Matrices, Oxford University Press, 1985.
[34] G. Grimvall, Thermophysical Properties of Materials, Elsevier, 1999.
[35] B. Fultz, J. Howe, Transmission Electron Microscopy and Diffractometry of Materials, Springer, 2012.
[36] J.H. Edgar (Ed.), Properties of Group III Nitrides, INSPEC, IEE, 1994.
[37] M.A. Blanco, A. Marco, D. Pandey, S. Romero, Evaluation of the bulk modulus and its pressure derivative using equations of state, Phys. Rev. B 63 (2001) 174103.
[38] P. Ravindran, L. Fast, P. Korzhavyi, B. Johansson, J. Wills, O. Eriksson, Density functional theory for calculation of elastic anisotropy in crystals, J. Appl. Phys. 84 (9) (1998) 4891.
[39] J.F. Shackelford, W. Alexander, Materials Science and Engineering Handbook, CRC Press, 2000.
[40] J.P. Poirier, Introduction to the Physics of the Earth's Interior, Cambridge University Press, 2000.
[41] A. Es-Smairi, S. Al-Qaisi, N. Sfina, A. Boutramine, H.R. Jappor, H.S. Alzahrani, A. H. Alfaifi, H. Rached, A.S. Verma, M. Archi, M.F. Rahman, DFT insights into the structural, stability, elastic, and optoelectronic characteristics of Na_2LiZF_6 (Z = Ir and rh) double perovskites for sustainable energy, J. Comput. Chem. 46 (2025) e70097, https://doi.org/10.1002/jcc.70097.
[42] G.K. Madsen, D.J. Singh, BoltzTraP. A code for calculating band-structure dependent quantities, Comput. Phys. Commun. 175 (1) (2006) 67–71.
[43] N.T. Hung, E.H. Hasdeo, A.R.T. Nugraha, M.S. Dresselhaus, R. Saito, Quantum effects in the thermoelectric power factor of low-dimensional semiconductors, Phys. Rev. Lett. 117 (3) (2016) 036602.
[44] Y. He, G. Galli, Microscopic origin of the reduced thermal conductivity of silicon nanowires, Phys. Rev. Lett. 108 (21) (2012) 215901.
[45] C.M. Jaworski, J. Yang, S. Mack, J.P. Heremans, Magnetic field dependence of the angular momentum flow in the phonon-driven spin seebeck effect, Phys. Rev. Lett. 106 (18) (2011) 186601.
[46] J. Carrete, L.J. Gallego, L.M. Varela, N. Mingo, Predicted low thermal conductivity in a new class of half-Heusler semiconductors, Phys. Rev. B 89 (5) (2014) 054310.
[47] X. Tang, L. Chen, T. Goto, T. Hirai, Thermoelectric properties of p-type $Bi2Te_3$-based alloys fabricated by mechanical alloying and spark plasma sintering, J. Appl. Phys. 97 (9) (2005) 093712.
[48] Y. Pei, X. Shi, A. Lalonde, H. Wang, L. Chen, G.J. Snyder, "convergence of electronic bands for high performance bulk thermoelectrics, Nature 473 (7345) (2011) 66–69.
[49] L. Lindsay, D.A. Broido, T.L. Reinecke, First-principles determination of ultrahigh thermal conductivity of boron arsenide: a competitor for diamond? Phys. Rev. Lett. 111 (2) (2013) 025901.
[50] J. Callaway, Model for lattice thermal conductivity at low temperatures, Phys. Rev. 113 (4) (1959) 1046.
[51] D.G. Cahill, W.K. Ford, K.E. Goodson, G.D. Mahan, A. Majumdar, H.J. Maris, R. Merlin, S.R. Phillpot, "nanoscale thermal transport, J. Appl. Phys. 93 (2) (2003) 793–818.
[52] G.A. Slack, The thermal conductivity of nonmetallic crystals, Solid State Phys. 34 (1979) 1.
[53] D.T. Morelli, V. Jovovic, J.P. Heremans, Intrinsically minimal thermal conductivity in cubic I-V-VI_2 semiconductors, Phys. Rev. Lett. 101 (2008) 035901.
[54] A.K. Kushwaha, S.P. Mishra, M.K. Vishwakarma, Shivali Chauhan, Hamad R. Jappor, R. Khenata, S. Bin Omran, Theoretical study of thermal conductivity, mechanical, vibrational and thermodynamical properties of $Ln_2Zr_2O_7$ (ln = La, Nd, Sm, and eu) pyrochlore, Inorg. Chem. Commun. 127 (2021) 108495, https://doi.org/10.1016/j.inoche.2021.108495.
[55] Abderrazak Boutramine, Samah Al-Qaisi, Norah Algethami, Salima Tastift, Amani H. Alfaifi, Hind Saeed Alzahrani, Hassan Chaib, Hamad Rahman Jappor, Rached Habib, First-principles investigation of K_2InSbZ_6 (Z= I, Br, Cl, F) eco-friendly halide double perovskites: structural, thermodynamic, optoelectronic, and thermoelectric properties for efficient energy harvesting applications, Phys. B Condens. Matter 711 (2025) 417280, https://doi.org/10.1016/j.physb.2025.417280.
[56] Samah Al-Qaisi, Nazia Iram, N. Sfina, Abderrazak Boutramine, Hamad Rahman Jappor, Amani H. Alfaifi, Hind Saeed Alzahrani, Rached Habib, Malak Azmat Ali, G. Murtaza, Comprehensive DFT study of K2TlZI6 (Z = Al, in) double perovskites: structural stability and potential for optoelectronic and thermoelectric energy harvesting, Phys. B Condens. Matter 710 (2025) 417239, https://doi.org/10.1016/j.physb.2025.417239.
[57] L. Azzouz, M. Halit, M. Rérat, R. Khenata, Ajaya K. Singh, M.M. Obeid, Hamad R. Jappor, Xiaotian Wang, Structural, electronic and optical properties of $ABTe_2$ (A = Li, Na, K, Rb, Cs and B = Sc, Y, la): insights from first-principles computations, J. Solid State Chem. 279 (2019) 120954, https://doi.org/10.1016/j.jssc.2019.120954.
[58] Hamad Rahman Jappor, Ali Obies Muhsen Almayyali, Hamza A. Mezher, Samah Al-Qaisi, S. Bin-Omran, Rabah Khenata, Prediction of 2D XC2N4 (X= Ti, Mo, and W) monolayers with high mobility as an encouraging candidate for photovoltaic devices, Surf. Interfaces 54 (2024) 105261, https://doi.org/10.1016/j.surfin.2024.105261.
[59] S. Bougaa, H. Baaziz, T. Ghellab, S. Adalla, L. Bouhdjer, Ş. Uğur, G. Uğur, Z. Charifi, Comprehensive DFT study of $ZnGe_{1-x}Si_xAs_2$ alloys: insights into structural, electronic, optical, and thermoelectric properties, Mater. Sci. Semicond. Process. 188 (2025) 109185, https://doi.org/10.1016/j.mssp.2024.109185.
[60] Ahmad Telfah, T. Ghellab, Z. Charifi, H. Baaziz, A.M. Alsaad, Sahar Abdalla, Wai-Ning Mei, R.F. Sabirianov, Enhancing the thermoelectric performance of $BiGa_2X_4$ (X=S, se) P-type semiconductors by optimizing charge carrier concentration or chemical potentials, J. Phys. Chem. Solid. 194 (2024) 112248, https://doi.org/10.1016/j.jpcs.2024.112248.
[61] T. Ghellab, Z. Charifi, H. Baaziz, Optimizing the thermoelectric behavior of novel Quaternary CoIrMnX (x=Sn, sb) alloys through chemical potential or carrier concentration doping, Solid State Commun. 389 (2024) 115594, https://doi.org/10.1016/j.ssc.2024.115594.
[62] A. Zikem, H. Baaziz, T. Ghellab, Z. Charifi, Fethi Soyalp, Electronic, optical, and thermoelectric properties of vacancy-ordered double perovskite K2SnX6 (X= Cl, Br, I) from first-principle calculations, Phys. Scripta 99 (3) (2024) 035917, https://doi.org/10.1088/1402-4896/ad1ad8.